[American Journal of Science, Vol. 310, November, 2010, P. 862–888, DOI 10.2475/09.2010.05]

STRATIGRAPHY OF THE PORT NOLLOTH GROUP OF NAMIBIA AND SOUTH AFRICA AND IMPLICATIONS FOR THE AGE OF NEOPROTEROZOIC IRON FORMATIONS

FRANCIS A. MACDONALD*, JUSTIN V. STRAUSS*, CATHERINE V. ROSE**, FRANCIS Ő. DUDÁS***, and DANIEL P. SCHRAG*

ABSTRACT. Uncertainties in the number and age of glacial deposits within the Port Nolloth Group have hindered both structural and stratigraphic studies in the Neoproterozoic Gariep Belt of Namibia and South Africa. These uncertainties are compounded by major lateral facies changes that complicate correlations locally. Herein, we report the results of integrated geological mapping, chemo- and litho-stratigraphic, and sedimentological studies that shed light on the age and stratigraphic architecture of the Port Nolloth Group. Particularly, we have distinguished an additional glacial deposit, herein referred to as the Namaskluft diamictite, which is succeeded by a *ca.* 635 Ma basal Ediacaran cap carbonate. This interpretation indicates that the stratigraphically lower, iron-bearing Numees diamictite is not Marinoan or Gaskiers in age, as previously suggested, but is instead a *ca.* 716.5 Ma Sturtian glacial deposit. A Sturtian age for the Numees Formation is further supported by the discovery of microbial roll-up structures in the dark limestone of the Bloeddrif Member that caps the diamictite. A re-evaluation of the age constraints indicates that all Neoproterozoic iron formations may be of Sturtian age, and thus indicative of secular evolution of the redox state of the ocean.

INTRODUCTION

The Port Nolloth Group (PNG) of South Africa and Namibia hosts glacial deposits, iron formations, mixed carbonate-siliciclastic rocks, enigmatic microbialites, economically significant sedimentary exhalative Pb-Zn deposits, and datable volcanic rocks (Rogers, 1915; Kröner, 1974; Frimmel, 2008). However, due to structural complexities and large lateral facies changes, stratigraphic correlations within the PNG have remained unclear. Particularly, much debate has centered around the number and age of the glacial deposits (Jasper and others, 2000; Frimmel, 2008). The most recent review of the stratigraphy of the PNG concludes that the Kaigas Formation (table 1) is a pre-Sturtian *ca.* 750 Ma glacial deposit, the Numees Formation and associated iron formation are *ca.* 580 Ma Gaskiers-age glacial deposits, and that both the *ca.* 716.5 Ma Sturtian and *ca.* 635 Ma Marinoan glaciations are missing (Frimmel, 2008). This interpretation has significant implications not only for the tectonic evolution of the Kalahari Craton, but also for the evolution of ocean chemistry. The presence of extensive iron formation is an important indicator of the redox state of the ocean, and thus constraining the temporal range of major iron deposits in Earth history is critical to a better understanding of the co-evolution of oxygen, climate, and life.

Previous studies have relied on regional lithostratigraphic correlations of the diamictites (for example Von Veh, 1993). However, such correlations can be compromised by complexities in the stratigraphy of glacial deposits: lateral facies changes are abundant, and glaciers access different sedimentary sources over time. In contrast, carbonate rocks that bound Neoproterozoic diamictites are likely to reflect conditions in a well-mixed ocean reservoir and have distinct geochemical and sedimentological

* Department of Earth and Planetary Sciences, Harvard University, 20 Oxford St., Cambridge, Massachusetts 02138, USA; fmacdon@fas.harvard.edu
** Department of Geosciences, Princeton University, Guyot Hall, Princeton, New Jersey 08544, USA
*** Department of Earth, Atmospheric and Planetary Sciences, Massachusetts Institute of Technology, 77 Massachusetts Avenue, Cambridge, Massachusetts, 02139, USA

TABLE 1

Generalized stratigraphy of the Port Nolloth Group, contrasting the stratigraphic scheme presented herein with that of Frimmel (2008)

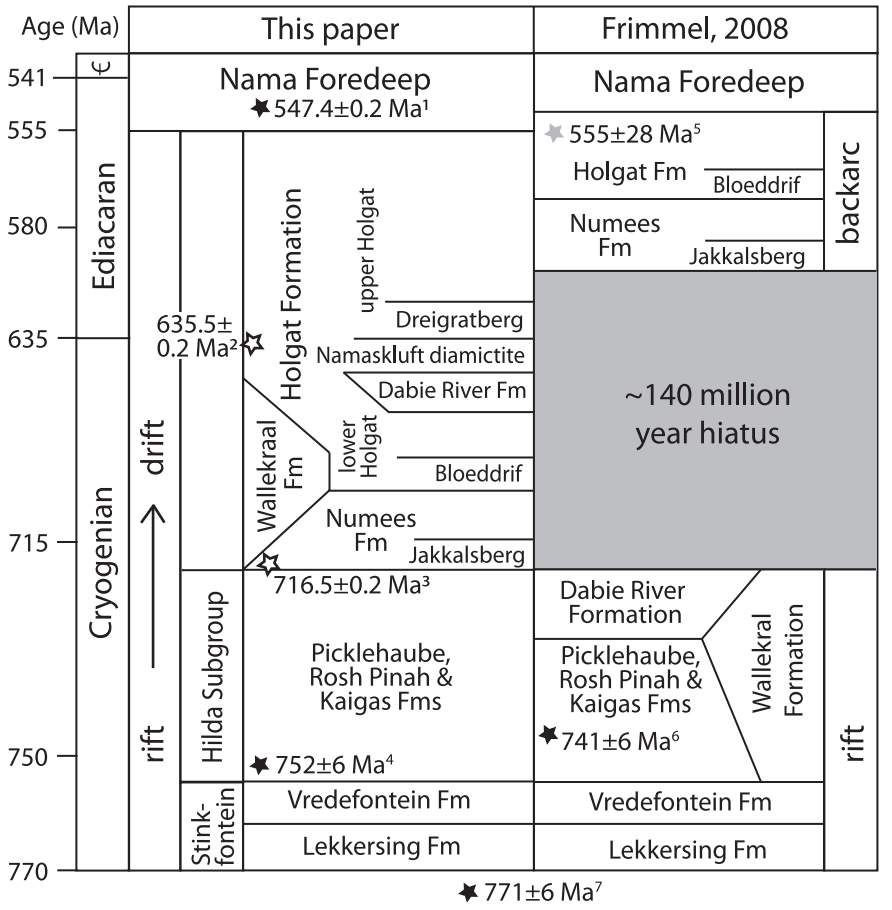

Numbered stars indicate stratigraphic positions of ages referred to in the text, filled stars are U-Pb zircon ages from within the stratigraphy, hollow stars are U-Pb zircon ages from the Sturtian and Marinoan glaciations on other continents, and gray stars are Pb-Pb carbonate ages.

[1]Bowring and others, 2007; [2]Hoffmann and others, 2004; [3]Macdonald and others, 2010; [4]Borg and others, 2003; [5]Foelling and others, 2000; [6]Frimmel and others, 1996; [7]Frimmel and others, 2001.

features that can be used for both local and global correlation (Hoffman and Schrag, 2002; Halverson and others, 2005). In this paper, we use carbon and strontium isotope chemostratigraphy linked to measured stratigraphic sections and geological mapping to test regional correlations and map relationships. We extend these regional correlations and construct a new age model for deposition of the PNG.

STRATIGRAPHIC SETTING

The Gariep Belt is a Pan-African/Brasiliano orogenic belt exposed on the western margin of the Kalahari Craton in southwestern Namibia and northwestern South Africa (Stowe and others, 1984). Folded strata in this Ediacaran to Cambrian transpressional orogen (Davies and Coward, 1982) include the PNG, which formed on the

Kalahari margin of the Adamastor Ocean after early Neoproterozoic to Cryogenian rifting (Jasper and others, 2000; Frimmel and others 2001), and the Nama Group, which was deposited in a foreland basin in response to the collision between the Congo, Kalahari, and Rio de la Plata cratons (Germs and Gresse, 1991). The PNG refers specifically to the Neoproterozoic stratigraphy in the Port Nolloth Zone, which is exposed on the autochthon and para-autochthon of the Gariep Belt (fig. 1), as distinguished from the allochthonous Mamora Terrane west of the Schakalsberge Thrust (Frimmel, 2008).

The PNG formed in NNW-SSE trending grabens, which post-date 771 ± 6 Ma granites of the Richtersveld suite (single grain Pb/Pb zircon evaporation age, Frimmel and others, 2001). A minimum age is provided by overlying foreland sedimentation of the Nama Group, which began by ~548 Ma (Grotzinger and others, 1995). The PNG in the South African portion of the Gariep Belt, including the Kaigas Series and the Numees Series, was first described by Rogers (1915), however diamictite was only identified in the Numees Series. The Kaigas diamictite was later distinguished from the Numees diamictite by De Villiers and Sohnge (1959). More recent mapping of the Gariep Belt, both on the South African side of the Orange River (Kröner, 1974; Von Veh, 1993) and the Namibian side (Martin, 1965b; McMillan, 1968; Jasper and others, 2000; Frimmel, 2008), has resulted in conflicting interpretations of the stratigraphy. Particularly, Von Veh (1993) and Frimmel (2008) introduced an array of thrust faults to accommodate their stratigraphic correlations. Our correlations suggest simpler structure (fig. 1), more akin to the earlier work of Rogers (1915), McMillan (1968), and Kröner (1974); however, the identification of the Namaskluft diamictite, which rests above the Numees Formation (table 1), allows many exposures previously correlated with the Kaigas Formation to be reassigned to the Numees Formation (fig. 1).

In contrast to previous studies of the PNG that focused on para-autochthonous and allochthonous exposures (for example Frimmel and others, 2002), we centered our litho- and chemo-stratigraphic studies on the least-deformed, most-autochthonous sections (fig. 1). Where possible we have retained the current stratigraphic nomenclature as reviewed by Frimmel (2008), but separated the Wallekraal and Dabie River Formations from the Hilda Subgroup and added informal members to distinguish the Namaskluft diamictite and Dreigratberg cap carbonate within the Holgat Formation (table 1). A critical difference in this stratigraphic scheme from previous work is that we place the Wallekraal and Dabie River Formations above the Numees diamictite.

STRATIGRAPHY OF THE PORT NOLLOTH GROUP

Stinkfontein and Hilda Subgroups

Deposition of the PNG commenced with the accumulation of approximately 800 m of coarse siliciclastic and bimodal volcanic rocks of the Stinkfontein Subgroup (Von Veh, 1993). These strata are succeeded by the Hilda Subgroup, which is subdivided into the Kaigas, Rosh Pinah, and Picklehaube Formations (table 1). The Kaigas Formation is up to 100 m thick and consists predominantly of subrounded, gravel- to boulder-sized basement clasts suspended in a matrix that ranges from argillite to feldspathic sandstone with complex lateral facies changes. The glacigenic origin of this diamictite remains questionable and depends on correlations with rocks that could alternatively be assigned to the Numees Formation. The Kaigas Formation is succeeded by the Rosh Pinah Formation, which consists of up to 850 m of arkosic sandstone, organic-rich shale, carbonate, and felsic volcanic rocks that were deposited in an actively rifting graben (Alchin and others, 2005). The volcanic rocks are thickest ~15 km north of Rosh Pinah near the Skorpion Mine (fig. 1), where they have also been referred to as the Spitzkop Formation. Rhyolite flows within the Rosh Pinah Formation contain zircons that have been dated at 752 ± 6 Ma (U/Pb zircon

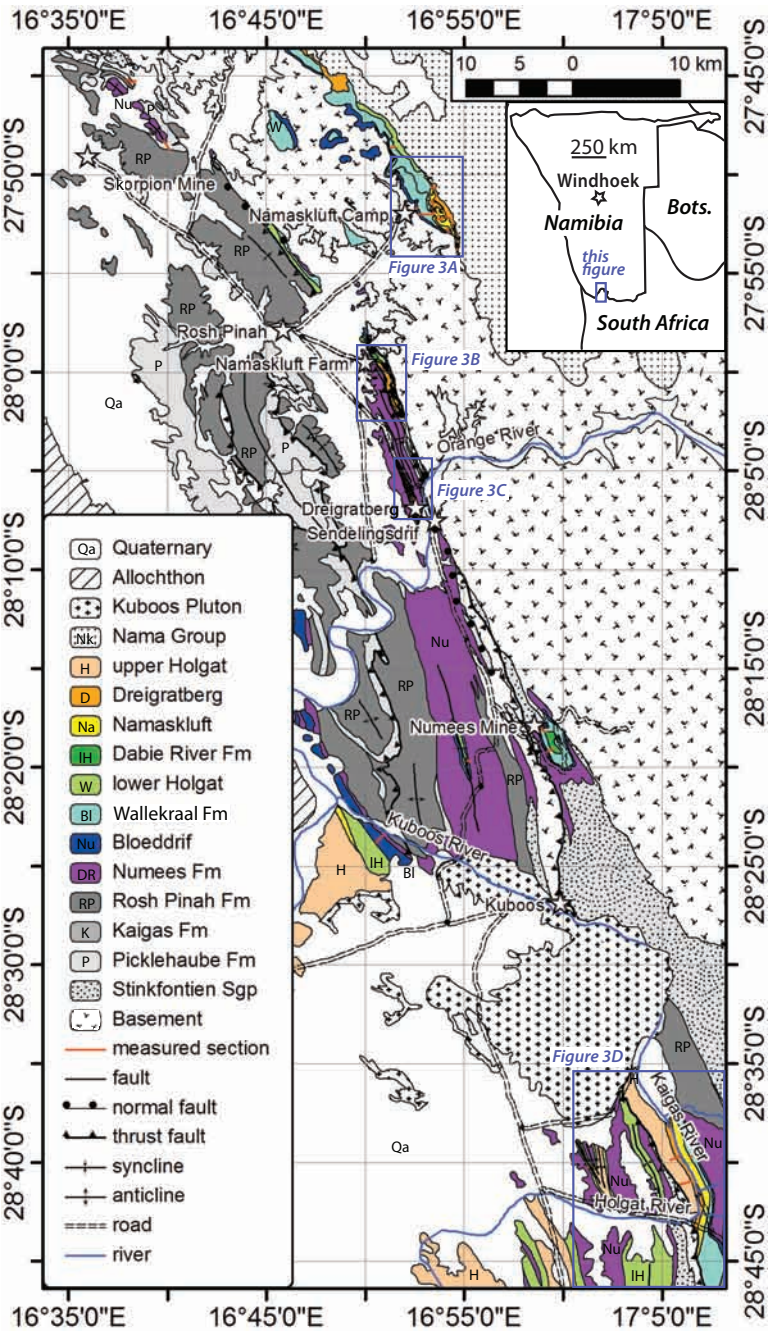

Fig. 1. Geological map of the Gariep Belt autochthon with inset of location map. Mapping southwest of Rosh Pinah modified from Von Veh (1993). Boxes mark the extent of the small-scale maps in figure 3. Stars mark locations discussed in the text.

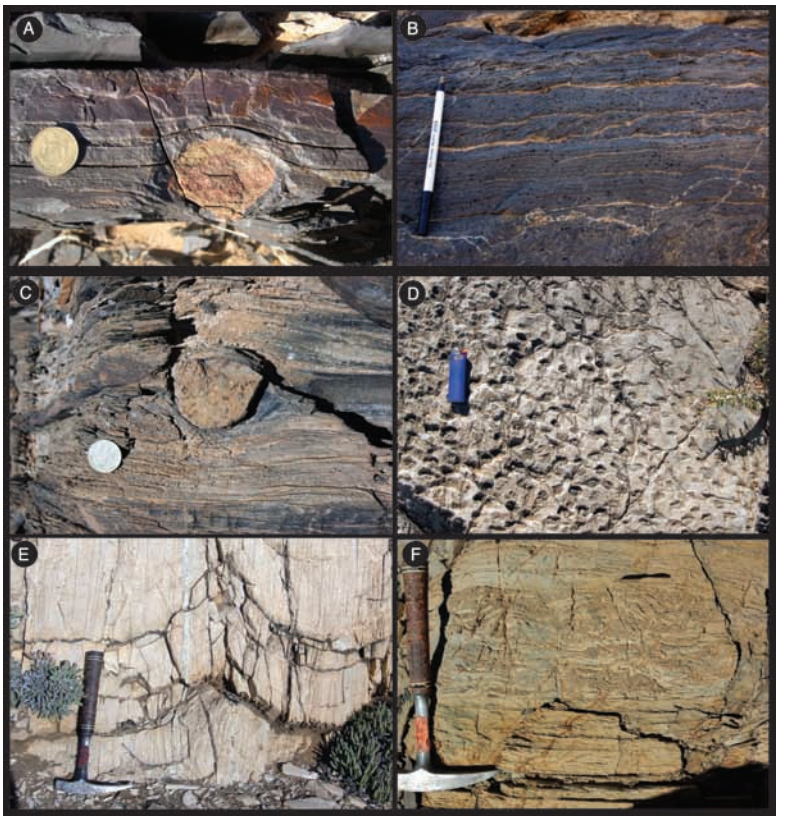

Fig. 2. Field photographs: (A) iron formation with dropstone in Numees Formation, northwest of Dreigratberg syncline, coin for scale is 2.5 cm in diameter; (B) microbialaminite of Bloeddrif member from Namaskluft Camp, ballpoint pen for scale; (C) carbonate dropstone in the Namaskluft diamictite at Dreigratberg, coin for scale is 2.0 cm in diameter; (D) tubestone stromatolites in plan view in the Dreigratberg cap carbonate on the top of the escarpment near Namaskluft Farm, lighter for scale; (E) giant wave ripples in the Dreigratberg cap carbonate on the top of the escarpment near Namaskluft Farm, 33 cm hammer for scale; (F) sheet-crack cements in the Dreigratberg cap carbonate at Dreigratberg, 33 cm hammer for scale.

evaporation age, Borg and others, 2003) and at 741 ± 6 Ma (Pb/Pb age, Frimmel and others, 1996).

The Picklehaube Formation is present predominantly west of Rosh Pinah, and is composed of greater than 200 meters of carbonate. A stratigraphic thickness is difficult to determine due to the strong deformation in these western exposures. On paleo-highs these carbonates consist of upward-shallowing parasequences capped by microbialaminates, including stromatolites and giant ooids (>0.5 cm diameter) that are lithologically very similar to those in the Dabie River Formation. In deeper-water settings, the Picklehaube Formation is composed of hundreds of meters of allodapic limestone.

Numees Formation

The Hilda Subgroup is overlain by the Numees Formation, which contains both massive and stratified glacial diamictites with dropstones (Rogers, 1915; Martin, 1965b) and the iron formation of the Jakkalsberg Member (Mb) (fig. 2A) (Frimmel and Von Veh, 2003). The Numees Formation is thickest in the syncline west of the Numees Mine (fig. 1) where it is estimated to be as much as 500 m thick (Frimmel and

Von Veh, 2003). Clasts within the diamictite are derived from all of the underlying stratigraphy and basement; outsized clasts reach several meters in diameter.

Holgat, Wallekraal, and Dabie River Formations

The Numees diamictite is capped by the Bloeddrif Member of the lower Holgat Formation, a dark gray laminated limestone that ranges in thickness from 1 to 120 m. This limestone unit contains microbial roll-up structures and abundant crinkly lamination that we interpret as sublittoral microbialaminite (fig. 2B), and it is commonly interbedded with thin grainstone and sandstone turbidite beds. The lower Holgat Formation consists of as much as 250 m of allodapic carbonate and argillite, including olistoliths of the Dabie River Formation.

The Wallekraal and Dabie River Formations have previously been included with the Hilda Subgroup (Frimmel, 2008). However, our mapping shows that these formations rest between the Numees and Namaskluft diamictites (figs. 1 and 3). On the autochthon, the Wallekraal Formation interfingers with the lower Holgat Formation (see description below in "Key Localities"), and consists predominantly of sandstone turbidites that were deposited in submarine channels. The Wallekraal Formation is distinguished from the Rosh Pinah Formation by the presence of boulder-sized olistoliths and coarse feldspathic grit. The Dabie River Formation is the shallow water equivalent of the lower Holgat Formation and consists of as much as 160 m of carbonate, including *conophyton* stromatolites, giant *ooids,* and *intraclast breccias.*

Throughout the Gariep Belt, the Namaskluft diamictite has either been overlooked or mis-mapped as the Numees diamictite. This has been a major source of stratigraphic confusion. The Namaskluft diamictite ranges from 5 to 240 m thick and consists of both massive and stratified diamictite units with clasts from all of the underlying stratigraphy and the basement. Outsized clasts and bed-penetrating dropstones suggest a glacial origin for the Namaskluft diamictite (fig. 2C). This diamictite is capped by the informally named Dreigratberg member of the upper Holgat Formation (table 1). In more proximal settings, the Dreigratberg member is up to 40 m thick and composed predominantly of buff-colored, fine-laminated, micropeloidal dolomite with stromatolite bioherms and giant wave ripples (figs. 2D and 2E). In deeper water settings, the Dreigratberg member is less than 5 m thick, and hosts sheet-crack cements (fig. 2F). These dolostones are overlain by as much as 400 m of allodapic carbonate, shale, and sandstone turbidites of the upper Holgat Formation. On the autochthon, the upper Holgat Formation is commonly cut out under the sub-Nama Group unconformity.

KEY LOCALITIES

Namaskluft Camp

At Namaskluft Camp (fig. 3A), the Stinkfontein Subgroup is missing and a diamictite lies directly on basement with a sharp erosional contact. This diamictite ranges from 0 to 35 m thick, and is composed predominantly of stratified diamictite. Clasts range in size from pebbles to boulders, and consist predominantly of granitic and gneissic basement with rare limestone and sandstone. The diamictite fills an ~8 km wide and ~1 km deep E-W oriented paleo-canyon (fig. 3A) and contains ripple cross-lamination with flow towards the west. A glacigenic origin for the diamictite is suggested by the presence of bed penetrating dropstones. This diamictite has previously been mapped as the Kaigas Formation (McMillan, 1968). However, we assign this diamictite to the Numees Formation because it is overlain by blue fine-laminated limestone that is lithologically and isotopically similar to the Bloeddrif Formation. These carbonate beds comformably grade into quartz sandstone turbidites (Bouma Ta-b) of the Wallekraal Formation in fining-upwards cycles ranging from <1 m to over

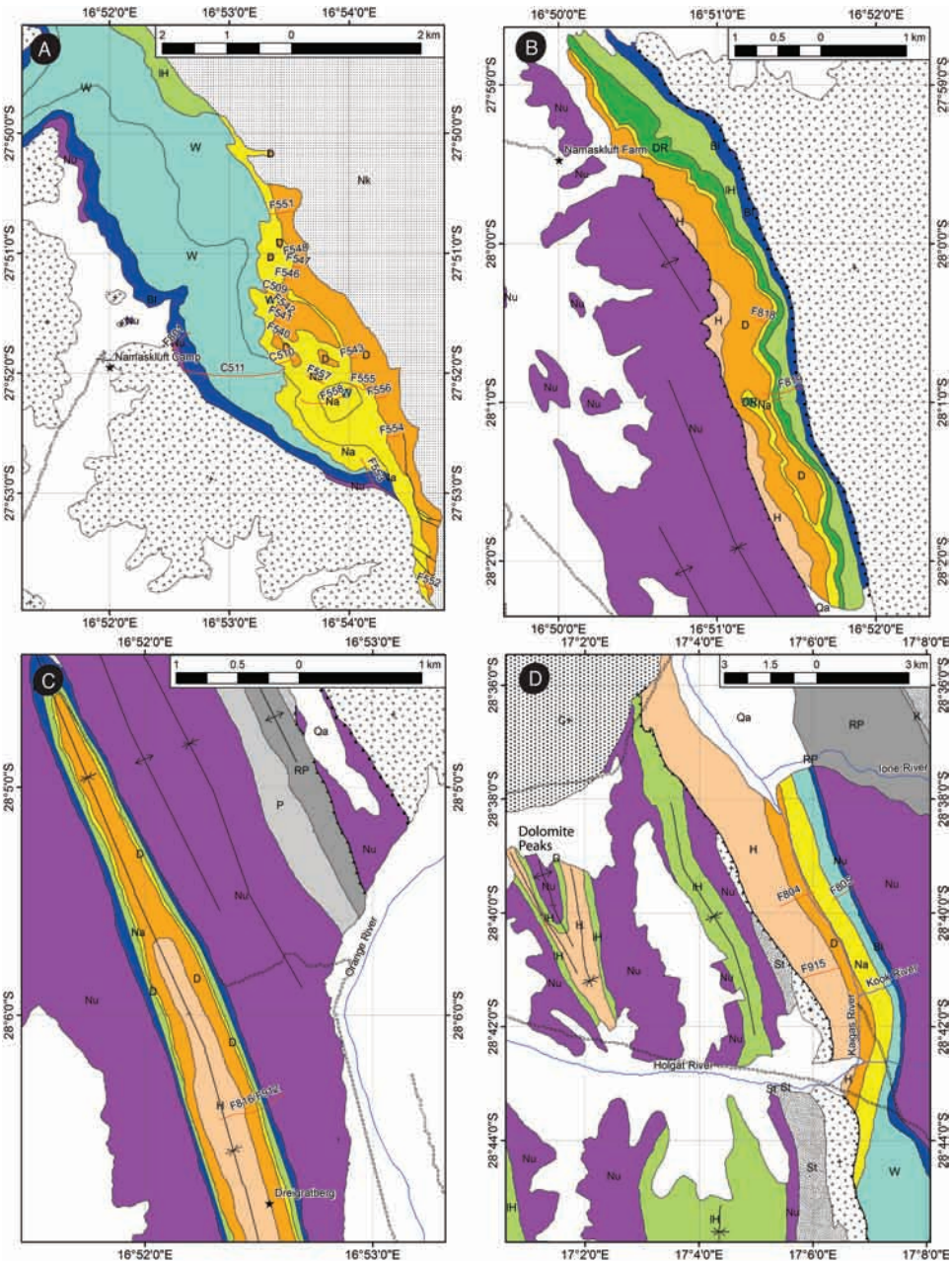

Fig. 3. Geological maps of (A) Namaskluft Camp, (B) Namaskluft Farm, (C) Dreigratberg, and the (D) Kaigas River region. Legend is the same as figure 1.

20 m. Scours and deep-water trough cross-beds are present that indicate flow to the west. Map relationships and measured sections indicate that the Wallekraal Formation thins dramatically both to the west and the east, consistent with the filling of a submarine channel that dissects a rift shoulder. The sandstone turbidites are up to

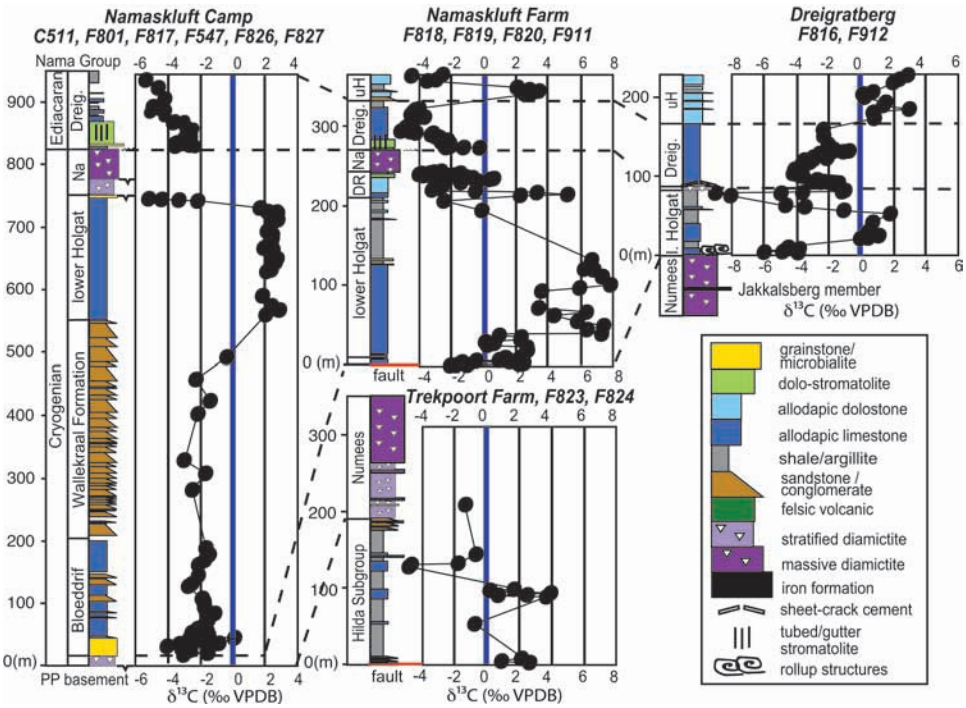

Fig. 4. Chemo-stratigraphic correlations of the PNG in Namibia. Trekpoort Farm is located near Skorpion mine. Locations of sections are in figures 1 and 3.

600 m thick and are succeeded by as much as 200 m of green argillite, allodapic limestone, and channelized debris flows dominated by very coarse subangular feldspathic grit with rafted angular limestone cobbles (fig. 4). The Wallekraal Formation grades upwards into micrite and marl of the lower Holgat Formation with carbonate olistostromes derived from the Dabie River Formation.

The overlying Namaskluft diamictite has an erosional base and rests on all of the underlying stratigraphy and basement. The diamictite is channelized and up to 240 m thick. Within the channel, the base of the diamictite consists of 20 to 70 m of green to purple laminated siltstone with granite boulder dropstones, limestone pebbles and gravel, and lenses of pebble conglomerate. This lower interval includes evidence of ice-grounding in the form of truncations, plowed clasts, and abundant soft-sedimentary deformation. The Namaskluft diamictite is succeeded by an additional ~90 m of sandstone matrix diamictite with lenses of carbonate pebble clasts, and intervals of green siltstone to marl matrix diamictite with granite boulder lonestones. These stratified diamictite units are overlain, across a sharp, erosional contact, by a massive diamictite that is up to 80 m thick and consists of clasts of limestone, dolomite, and sandstone in a chocolate brown calc-arenite matrix. The upper meter of the Namaskluft diamictite has a laminated matrix with bed-penetrating dropstones, flame structures, and festoon cross-lamination. The Namaskluft diamictite is overlain by a fine-laminated, buff-colored micropeloidal dolomite with low angle cross-stratification that we assign to the Dreigratberg Member. Outsized clasts occur in the lower 0.5 m of the Dreigratberg Member. The cap dolostone is up to 30 m thick and also contains giant wave ripples and tubestone stromatolites (Corsetti and Grotzinger, 2005). It is overlain by >300 m of upper Holgat strata consisting of pink to light gray, allodapic

limestone and siltstone with occasional hummocky cross stratification that are preserved under the sub-Nama unconformity.

Namaskluft Farm

The carbonates exposed on Namaskluft Farm (fig. 3B) are stratigraphically above the Numees diamictite and below the Namaskluft diamictite, and thus should be included with the lower Holgat Formation. On the easternmost exposures, limestone and a thin, laterally discontinuous diamictite rest with a tectonic contact against crystalline basement. We interpret this contact as a syn-sedimentary normal fault. Above the diamictite are ~120 m of limestone rhythmite, ~80 m of argillite with carbonate olistostromes, and an additional ~30 m of massive carbonate grainstone with stromatolite bioherms (fig. 4). The stromatolites are sharply overlain by the Namaskluft diamictite, which consists of ~30 m of carbonate matrix diamictite with predominantly sub-rounded carbonate cobbles and boulders with rare sandstone clasts. The Namaskluft diamictite is capped by ~15 m of buff-colored dolomite with bioherms that are filled with irregular cements, herein assigned to the Dreigratberg Member. This is overlain by an ~50 m thick transgressive sequence of folded pink limestone rhythmite and an additional ~50 m of mixed allodapic carbonate and siliciclastic rocks of the upper Holgat Formation. To the west, the Holgat Formation is truncated by a thrust fault that places the Fe-rich Numees Formation structurally above the Holgat Formation (fig. 3B). To the south, along the Orange River, this thrust cuts out the Holgat Formation, and the Hilda Subgroup is present in the hanging wall in the core of an anticline, which is thrust onto a sliver of diamictite that is most likely the Numees Formation (fig. 3C). In contrast to previous mapping, this new unit assignment leads to kinematically feasible structures. Moreover, the northern extensions of these structures comprise an exposure of limestone and diamictite in the footwall of a thrust on the east side of Rosh Pinah Mountain that have previously been assigned to the Pickelhaube and Kaigas Formations (Von Veh, 1993; Alchin and others, 2005; Frimmel, 2008). A simpler interpretation is that these units belong to the Wallekraal, lower Holgat, and Numees Formations.

Dreigratberg

At Dreigratberg, the Holgat Formation is exposed at the center of a simple syncline surrounded by the Numees diamictite and its associated iron formation (fig. 3C). This correlation is supported by the presence of a fine-laminated, dark gray cap limestone with sub-littoral microbialaminite and roll-up structures that rests on the diamictite. The cap is ~10 m thick and is succeeded by ~50 m of argillite and marl (fig. 4). These marls grade into a stratified diamictite with rare, subrounded carbonate and sandstone cobble lonestones. We assign this stratified diamictite to the Namaskluft diamictite because it is capped by 5 m of white dolomite with bed-parallel cements and an additional ~50 m of pink limestone, characteristic of the upper portion of the Dreigratberg cap carbonate. In the core of the syncline is an additional ~250 m of allodapic carbonate, shale and wackestone of the upper Holgat Formation.

Numees Mine to Bloeddrif

At Numees Mine, the Stinkfontein Subgroup is unconformably overlain by up to 100 m of diamictite. This diamictite is capped by more than 20 m of blue-gray limestone and ~300 m of arkosic turbidites. The limestone and arkose units are indistinguishable from those exposed at Namaskluft Camp and are assigned to the Bloeddrif Member and Wallekraal Formation respectively. The upper ~100 m of strata exposed on the escarpment above the Numees Mine consist of a poorly sorted, carbonate-clast conglomerate (fig. 5) with boulder olistoliths of giant ooids assigned to the Dabie River Formation (fig. 5).

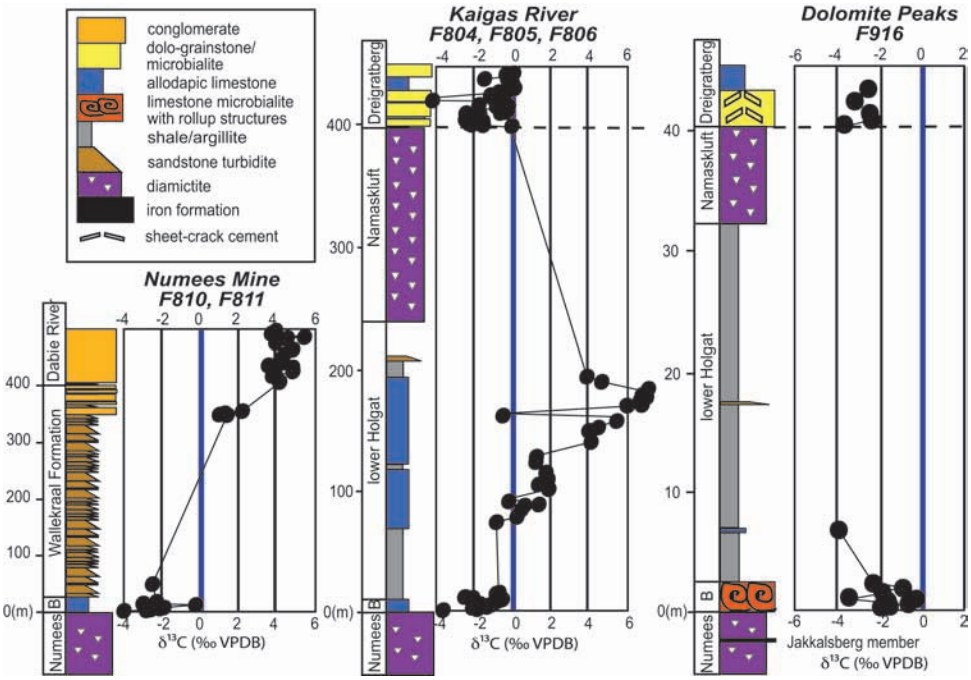

Fig. 5. Chemo-stratigraphic correlations of the PNG in South Africa. Locations of sections are in figures 1 and 3.

The type locality of the Numees Formation is located in South Africa in the broad syncline ~10 km due west of Numees Mine (fig. 1), where it is >500 m thick and consists predominantly of a massive diamictite with subrounded clasts of granite, quartzite, schist, and dolomite in a dark colored, ferruginous, fine- to medium-grained quartz-mica schist matrix (Frimmel and Von Veh, 2003). The diamictite is interbedded with a ferruginous feldspathic arenite and banded iron formation of the Jakkalsberg Member. In the core of the syncline the Numees Formation is capped with a dark gray, fine laminated limestone that grades upwards into limestone marl and metapelite. This exposure can be correlated with the type section of the Bloeddrif Member located ~10 km to the west.

Kaigas River

On the autochthon, near the Kaigas River (fig. 3D), the Numees Formation is >1 km thick and composed of a sandstone matrix diamictite with boulder-sized clasts of crystalline basement rocks and sandstone. This diamictite is interbedded with thick-bedded sandstone turbidites of the Wallekraal Formation. It has previously been mapped as the Kaigas Formation with several thrust repetitions (Von Veh, 1993). However, our mapping has demonstrated that the sandstone bodies are channelized and interbedded with the diamictite, and like Kröner (1974), we conclude that there are no such thrust repetitions. Moreover, the diamictite is capped by the Bloeddrif Member, which consists of 12 m of dark gray limestone rhythmite and microbialaminite that is succeeded by ~200 m of argillite and marl.

On the autochthon, the Namaskluft diamictite is typically massive and consists of cobble-sized carbonate and sandstone clasts in a sandstone to argillite matrix. It is ~100 m thick and poorly exposed. Stratified units with bed-penetrating dropstones are

also present. The Namaskluft diamictite is capped by the Dreigratberg Member, which consists of up to 200 m of light gray to buff-colored dolomite. The Dreigratberg Member is formed predominantly of recrystallized grainstone, but also contains giant wave ripples and massive stromatolite bioherms. The transgressive sequence above the Dreigratberg Member consists of pink marl and rhythmite with occasional hummocky cross-stratification, as well as mixed carbonate and sandstone in well-developed parasequences. We interpret these beds as a proximal facies of the upper Holgat Formation.

On the para-autochthon, the Stinkfontein Subgroup rests on basement and is beveled by a diamictite (fig. 3D). We suggest this diamictite is the Numees Formation because it is capped by a limestone that is indistinguishable from the Bloeddrif Member. To the west, in the Dolomite Peaks, the Jakkalsberg iron formation is present in the Numees Formation and the overlying Bloeddrif Member contains microbial roll-up structures, reminiscent of Sturtian-age cap carbonates elsewhere (Hoffman and Schrag, 2002). The Bloeddrif Member is less than 3 m thick and is succeeded by over 30 m of argillite and marl (fig. 5). In the Dolomite Peaks, the lower Holgat Formation grades into a stratified diamictite with rare carbonate lonestones. This unit, assigned to the Namaskluft diamictite, is capped by ~5 m of dolomite with sheet-crack cements. An additional ~100 m of allodapic carbonate and argillite are present in the Dolomite Peaks above the Dreigratberg Member, but these units are highly folded and difficult to measure with confidence.

CHEMOSTRATIGRAPHY

Previous Studies

Carbon, oxygen, and strontium isotopes were previously reported from Dreigratberg and Namaskluft Farm in Namibia, and from near Numees Mine and Bloeddrif in South Africa (Foëlling and Frimmel, 2002). Our mapping suggests that the data previously attributed to the Picklehaube Formation is actually from strata between the Numees and Namaskluft diamictites (Frimmel, 2007), and should thus be assigned to the lower Holgat Formation.

Frimmel and Foëlling (2004) report two additional sections of the Bloeddrif Member from the Kaigas River and from the Bloeddrif type locality along the Kuboos River (fig. 1), but the section from the Kaigas area is actually from the Dreigratberg cap carbonate.

Carbon Isotopes

Above the lower diamictite at Namaskluft Camp, $\delta^{13}C$ values in the Bloedriff Member start near −6 permil and increase to −2 permil over ~30 m with considerable scatter (fig. 4). A similar pattern is present in the Bloedriff Member at Numees Mine (fig. 5). In more distal, condensed sections, carbon isotope values in the Bloeddrif Member rise from −6 permil to 0 permil in ~10 m of strata. The succeeding $\delta^{13}C$ values in the lower Holgat Formation describe an arc with values increasing up to +8 permil before plummeting into a negative anomaly (fig. 4). At Namaskluft Camp, Namaskluft Farm and Dreigratberg, this pronounced negative $\delta^{13}C$ anomaly is developed under the Namaskluft diamictite with values as low as −9 permil.

The Dreigratberg Member at Namaskluft Camp, Namaskluft Farm, and Dreigratberg all display a sigmoidal $\delta^{13}C$ profile with values decreasing from −2 permil to below −5 permil. In the Kaigas River region, $\delta^{13}C$ values in the Dreigratberg cap carbonate vary between −2 permil and 0 permil (fig. 5).

Strontium Isotopes

We report 23 new $^{87}Sr/^{86}Sr$ measurements (table 2). Unlike Halverson and others (2007), we are unable to define a reliable alteration cutoff based on Sr concentration.

TABLE 2

Strontium isotope and trace element data from the Port Nolloth Group

Sample	Locality	Unit	Age (Ma)	$^{87}Sr/^{86}Sr$	$\delta^{13}C$	$\delta^{18}O$	Sr (ppm)	Mn (ppm)	Mg (%)	Mn/Sr	Mg/Sr
F539_15.6	Namaskluft Camp	Dreigratberg	<635	0.70824	-3.72	-12.32	370.1	322.3	0.3	0.9	9.4
F539_14.0	**Namaskluft Camp**	**Dreigratberg**	**<635**	**0.70773**	**-3.34**	**-11.69**	**299.2**	**331.5**	**0.3**	**1.1**	**11.1**
F539_11.8	Namaskluft Camp	Dreigratberg	<635	0.70817	-3.59	-12.67	625.6	287.7	0.2	0.5	3.8
F539_8.3	Namaskluft Camp	Dreigratberg	<635	0.70794	-3.69	-13.83	727.0	447.6	0.2	0.6	3.1
F539_6.3	Namaskluft Camp	Dreigratberg	<635	0.70846	-3.85	-14.16	596.2	699.4	0.3	1.2	4.3
F539_3.4	Namaskluft Camp	Dreigratberg	<635	0.70831	-3.81	-15.01	1034.2	1421.9	0.3	1.4	2.6
F539_3.0	Namaskluft Camp	Dreigratberg	<635	0.70930	-	-	404.6	859.8	0.2	2.1	3.9
F826_270	Namaskluft Camp	lower Holgat	635-716	0.70831	2.85	-10.24	415.0	28.0	0.3	0.1	7.5
F826_259	Namaskluft Camp	lower Holgat	635-716	0.70815	2.86	-10.32	590.0	28.0	2.1	0.0	36.1
F826_229	Namaskluft Camp	lower Holgat	635-716	0.70917	2.51	-10.42	514.0	96.0	0.1	0.2	2.7
F826_210	Namaskluft Camp	lower Holgat	635-716	0.70984	2.54	-11.46	624.0	223.0	0.1	0.4	1.8
F826_193	Namaskluft Camp	lower Holgat	635-716	0.70879	2.78	-11.18	618.0	63.0	0.1	0.1	1.8
F819_40	Namaskluft Farm	lower Holgat	635-716	0.70861	0.22	-8.23	196.0	21.0	0.5	0.1	23.0
F816_76	Dreigratberg	lower Holgat	635-716	0.71701	-9.00	-13.56	397.0	285.0	0.3	0.7	8.1
F816_18.5	Dreigratberg	lower Holgat	635-716	0.71380	0.01	-14.43	419.0	420.0	0.2	1.0	5.0
F816_1.8	Dreigratberg	Bloeddrif	635-716	0.72858	-4.83	-15.18	378.0	239.0	2.5	0.6	66.4
F816_1.1	Dreigratberg	Bloeddrif	635-716	0.72912	-5.98	-15.71	597.0	109.0	1.2	0.2	20.8
F801_50.7	Namaskluft Camp	Bloeddrif	635-716	0.70732	-2.80	-10.62	571.0	72.0	0.1	0.1	1.6
F801_45	**Namaskluft Camp**	**Bloeddrif**	**635-716**	**0.70718**	**-3.26**	**-10.62**	**749.0**	**132.0**	**0.1**	**0.2**	**1.5**
F801_38.7	**Namaskluft Camp**	**Bloeddrif**	**635-716**	**0.70714**	**-2.24**	**-11.72**	**489.0**	**100.0**	**0.1**	**0.2**	**1.6**
F801_32.3	Namaskluft Camp	Bloeddrif	635-716	0.70843	-4.22	-16.60	779.0	33.0	0.1	0.0	1.4
F823_128	Trekpoort Farm	Picklehaube	>716	0.72374	-4.70	-11.61	357.0	77.0	3.7	0.2	102.8
F823_127.5	Trekpoort Farm	Picklehaube	>716	0.73059	-4.78	-13.41	281.0	68.0	3.6	0.2	128.8

The most reliable data are in bold (see text for discussion).

Mn/Sr, Mg/Sr, and $\delta^{18}O$ values provide a rough guide to the extent of alteration, but we again cannot define a meaningful cutoff value in any of these proxies. We distinguish "most reliable" data based on the absolute $^{87}Sr/^{86}Sr$ value, because diagenetic overprinting usually increases $^{87}Sr/^{86}Sr$ (Banner and Hanson, 1990), and consequently, unradiogenic values (here less than 0.7080) are likely near primary values.

DISCUSSION

Regional and Global Correlations

Previous age constraints on the Kaigas and Rosh Pinah Formations of 752 ± 6 Ma (Borg and others, 2003) and 741 ± 6 Ma (Frimmel and others, 1996), respectively, come from exposures on Trekpoort Farm, near Skorpion Mine (fig. 1), where the Kaigas Formation is tectonically dismembered. At this locality, the Hilda Subgroup is overlain, in the core of the syncline, by a thick, Fe-rich diamictite that we have assigned to the Numees Formation. That is, the *ca.* 750 Ma ages are from volcanic rocks that are stratigraphically below the Numees diamictite. This interpretation is consistent with maximum age constraints on the Sturtian glaciation of 726 ± 1 Ma in Oman (Bowring and others, 2007), 725 ± 10 Ma on the Tarim Block (Xu, 2009), and 717.43 ± 0.14 in the Yukon (Macdonald and others, 2010). Therefore, the Kaigas Formation was deposited prior to the *ca.* 716.5 Ma Sturtian glaciation (Macdonald and others, 2010). Moreover, a glacial origin of the Kaigas Formation is highly questionable and is based largely on miscorrelations with the glacigenic Numees Formation.

A Gaskiers age has been proposed for the Numees diamictite (Frimmel and Foëlling, 2004; Frimmel, 2008) on the basis of a 555 ± 28 Ma Pb/Pb carbonate age on the Bloeddrif Member (Foëlling and others, 2000), and radiogenic Sr isotope values ($^{87}Sr/^{86}Sr > 0.7082$; Foëlling and Frimmel, 2002). However, this age and the Pb/Pb carbonate dating technique are unreliable because Pb is mobile in carbonate (Sumner

and Bowring, 1996). Radiogenic Sr isotope compositions may, in part, be due to sample preparation procedures that do not attempt to remove clay- and surface-bound Sr (compare methods of Derry and others, 1989 and Asmerom and others, 1991, with Gao and others, 1996, and Bailey and others, 2000), and to disturbance of the Sr system during Pan-African orogenesis. Our $^{87}Sr/^{86}Sr$ data for the Bloeddrif Member are from the least deformed sections on the autochthon, whereas Foëlling and Frimmel (2002) reported results from the highly tectonized exposures on the para-autochthon at the Bloeddrif type section. Our data for the Bloeddrif Member indicate $^{87}Sr/^{86}Sr$ as low as 0.7071, a value that is most consistent with marine Sr isotopic compositions before the *ca.* 635 Ma Marinoan glaciation (Sawaki and others, 2010), and similar to $^{87}Sr/^{86}Sr$ values from Sturtian cap carbonates in the Rasthof Formation of northern Namibia (Halverson and others, 2007) and the Tsaagan Oloom Formation of Mongolia (Brasier and others, 1996).

This new geochemical dataset is supported by sedimentological and chemostratigrahic data from the Bloeddrif Member, which are characteristic of Sturtian-age cap carbonates globally. This unit consists of dark colored, fine-laminated limestone with distinct microbial roll-up structures, and a sharp negative carbon isotope anomaly (Hoffman and Schrag, 2002). Moreover, an additional diamictite, herein referred to as the Namaskluft diamictite, is stratigraphically above the Numees diamictite and the Bloeddrif Member in multiple sections. This uppermost diamictite is capped by the Dreigratberg member, a micro-peloidal dolostone with low-angle cross-lamination, tubestone stromatolites, and giant wave ripples. Carbon isotope analyses through the Dreigratberg member display a sigmoidal profile with a nadir at ~ -5 permil. These sedimentological and geochemical features are characteristic of basal Ediacaran cap carbonates globally (Hoffman and others, 2007). Our Sr isotopic data for the Dreigratberg member show a minimum $^{87}Sr/^{86}Sr$ near 0.7077, which is consistent with basal Ediacaran marine Sr compositions (Halverson and others, 2007; Sawaki and others, 2010). Thus, the Numees diamictite is stratigraphically between the *ca.* 750 Ma Kaigas Formation and the *ca.* 635 Ma Namaskluft diamictite. Given this relationship, we suggest that the Numees Formation and associated iron formation are correlative with the *ca.* 716.5 Ma Sturtian glaciation. As such, the *ca.* 750 Ma ages from the Hilda Subgroup are maximum age constraints on the Sturtian glaciation.

In this new stratigraphic framework, the composite $\delta^{13}C$ curve from the PNG can be used to construct an age model (fig. 6) in which the negative $\delta^{13}C$ anomaly beneath the Numees diamictite is correlative with the pre-Sturtian Islay anomaly (Calver, 1998; Halverson, 2006; Prave and others, 2009), the negative $\delta^{13}C$ anomaly in the Bloeddrif Member is correlative with the Rasthof anomaly that is present in Sturtian cap carbonates around the world (Yoshioka and others, 2003; Halverson and others, 2005), the negative $\delta^{13}C$ anomaly below the Namaskluft diamictite is correlative with the Trezona anomaly that is below the Marinoan glaciation at several localities globally (McKirdy and others, 2001; Hoffman and Schrag, 2002; Halverson and others, 2005), and the negative $\delta^{13}C$ anomaly in the Dreigratberg cap carbonate is equivalent to the Maieberg anomaly in basal Ediacaran cap carbonates (Kennedy, 1996; Halverson and others, 2005) (fig. 6). These new correlations demonstrate that the carbon isotope chemostratigraphy of the Port Nolloth Group is consistent with global composite curves. Claims to the contrary (Frimmel, 2010) are a product of regional stratigraphic miscorrelations.

Implications for the Micropaleontology Record

Microfossils have been described previously in the PNG (Gaucher and others, 2005) and have been cited to support a Gaskiers age of the Numees Formation (Frimmel, 2008). *Bavlinella* was identified in samples from organic rich marl and shale in the Dreigratberg section that were assigned to the Picklehaube and Wallekraal

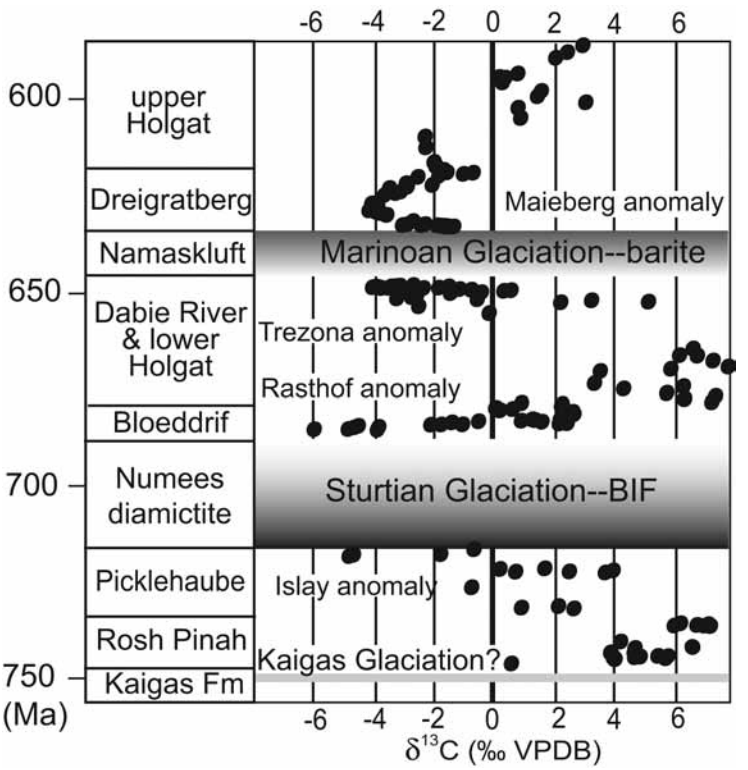

Fig. 6. Composite carbon isotope curve of the PNG plotted against time. Boxes representing the glacial events are faded to lighter shades to represent the uncertainty in the maximum age constraint for the Sturtian glaciation and for the minimum age constraint for the Marinoan glaciation. Pre-Numees data are from the Skorpion mine area and post-Numees data are from Namaskluft Farm and Dreigratberg. Carbon isotope anomalies are discussed in text.

Formations (Gaucher and others, 2005). In our new stratigraphic framework, the entire Holgat Formation is exposed in the Dreigratberg section, and it is unclear if these samples were collected above or below the Namaskluft diamictite. Thus, these *Bavlinella* specimens are constrained to post-date the Sturtian-age (*ca.* 716.5 Ma) Numees Formation. The range of *Bavlinella* is not well constrained as an index fossil (Knoll and others, 2006), and its presence does not provide any further constraints on the age of the PNG stratigraphy.

Other microfossils identified in the PNG consist of large colonies of cells extracted from the upper Holgat Formation at Witputs Farm (north of map area in fig. 1) (Gaucher and others, 2005). These samples are from marl and shale above a diamictite and buff-colored cap dolomite with stromatolite bioherms that is indistinguishable from the Dreigratberg cap carbonate near Namaskluft Camp. Thus, the underlying diamictite unit should be assigned to the Namaskluft diamictite rather than the Numees Formation, and the microfossils are in post-635 Ma strata. This age assignment is consistent with the micropaleontology; the clusters of cells described are similar to forms in the post-635 Ma Doushantuo Formation in South China (Xiao and others, 2004), but again the ranges of such forms are not well constrained as index fossils.

TABLE 3

Neoproterozoic iron formations and their respective age constraints

Location	Paleocontinent	Host strata	Age	Constraint	#	Reference
NW Canada	Laurentia	Rapitan Gp*	Sturtian	716.5 Ma*	1 of 2	Young, 1976; Yeo, 1981; Klein and Beukes, 1993
SW US	Laurentia	Surprise Fm	Sturtian	pre-635 Ma	1 of 2	Prave, 1999; Corsetti and Kaufman, 2003
Urals	Baltica	Tany Fm	Sturtian	pre-635 Ma	1 of 2	Chumukov, 2007
Australia	Australia	Sturt Fm	Sturtian	pre-660 Ma	1 of 2	Preiss, 1987; Lottermoser and Ashley, 2000
S. China	S. China	Chag'an	Sturtian	725-655 Ma	1 of 2	Jiafu and others, 1987; Wang and Li, 2003
N. Namibia	Congo	Chuos Fm	Sturtian	740-635 Ma	1 of 2	Martin 1965; Badenhorst, 1988; Clifford, 2008
Erzin	Tuva-Mongolia	Maikhan Ul	Sturtian	776-635 Ma	1 of 2	Ilyin, 2009; Macdonald and others, 2009
S. Africa	Kalahari	Numees Fm	Sturtian	750-635 Ma	2 of 3?	This paper; Frimmel and Von Veh, 2003
Brazil	Amazonia	Jacadigo Gp	?	pre-550 Ma	1?	Dorr, 1945; Urban and others, 1992; Klein and Ladeira, 2004
Iran	Iran	Rizu Fm	?	?	1?	Kianian and Khakzad, 2008

* Includes 716.5 Ma Upper Mt. Harper and Tindir Groups, Macdonald and others, 2010.

is the number of glacial deposits in the succession in which iron formation occurs, numbered from oldest to youngest.

Structural and Tectonic Implications

The new mapping and correlations presented herein suggest a much simpler structure in the Gariep Belt than envisioned by some previous geologists who invoked thrust repetitions to reconcile stratigraphic inconsistencies (for example, Von Veh, 1993). Broadly, the Numees Formation is thickest on the hanging-wall of a west dipping, syn-sedimentary normal fault that defines the eastern margin of the Rosh Pinah graben and the para-autochthon. To the west, the para-autochthon is folded into an approximately 20 km wide anticline-syncline pair, with the Hilda Subgroup well-developed in the axis of the Rosh Pinah graben.

Recently, it has been suggested that the upper portion of the PNG includes both a successor back-arc basin and the beginnings of foreland deposition (Frimmel and Foëlling, 2004; Basei and others, 2005; Frimmel, 2008). This interpretation stems from the proposed Gaskiers-age of the Numees Formation which implies a ~150 Myr hiatus in the PNG and an Ediacaran tectonic reactivation of the margin to accommodate the Holgat Formation. Our new age model (fig. 6) makes these hypothesized tectonic events unnecessary and points to a much simpler evolution of the margin. Particularly, we suggest that rifting began between ~770 and ~750 Ma forming the Rosh Pinah graben and the margin remained tectonically active through the deposition of the Numees diamictite at *ca.* 716.5 Ma. In this model, the Holgat Formation was deposited on a thermally-subsiding passive margin, which was only reactivated in the latest Ediacaran with the foredeep deposition of the Nama Group at the onset of the Gariep orogeny.

Neoproterozoic Iron Formations and Oceanic Redox

Neoproterozoic iron formations are present on nine separate paleocontinents marking a return to the stratigraphic record after an absence of over one billion years (Klein and Beukes, 1993) (table 3). The new age assignment of the Numees Formation is of particular interest because it hosts the iron formation of the Jakkalsberg Member

(fig. 5) (Frimmel and Von Veh, 2003). In addition to the iron formations of the Jacadigo Group in the Urucum District of Brazil and Bolivia (Dorr, 1945; Urban and others, 1992; Trompette and others, 1998; Klein and Ladeira, 2004), and the Rizu Formation of Iran (Kianian and Khakzad, 2008), the Jakkalsberg Member of the Numees Formation was previously considered one of three Neoproterozoic iron formations that do not belong to the Sturtian glaciation (Frimmel, 2008; Hoffman and Li, 2009). As discussed above, a Gaskiers age of the Numees diamictite is espoused by several authors, whereas Hoffman and Li (2009) mis-assigned the Jakkalsberg Member to the Kaigas Formation and correlated the cratonic Jacadigo Group with the Puga Formation in the adjacent Paraguay fold belt (Alvarenga and Trompette, 1992; Nogueira and others, 2003). The Puga Formation is overlain with a typical Marinoan-type cap dolostone (Font and others, 2006; Nogueira and others, 2007; Alvarenga and others, 2008); however, no cap carbonate is preserved on the Jacadigo Group, and the contact with the overlying Ediacaran-age Corumbá Group is not exposed and possibly unconformable. Moreover, the age constraints on the Rizu Formation are so poor that any assignment is arbitrary (Kianian and Khakzad, 2008). Thus, it is possible that all Neoproterozoic iron formations are of a *ca.* 716.5 Ma Sturtian age.

Iron formation requires anoxic deep waters and either S:Fe flux ratios < 2 to enable reduced Fe to travel freely in solution without being titrated out as pyrite during bacterial sulfate reduction (BSR) (Canfield, 2004), or insufficient organic substrate for BSR (Mikucki and others, 2009). A low S:Fe flux into the ocean may have been accomplished by diminished sulfate input from the continents during glaciation (Canfield, 2004), and by lowered S:Fe flux in hydrothermal vent fluids due to the decrease in hydrostatic pressure resulting from glacioeustatic sea level fall (Kump and Seyfried, 2005). Moreover, ice cover may have caused primary productivity to crash, thereby limiting BSR.

Interestingly, while Neoproterozoic iron formations are predominately hosted by Sturtian glacial deposits, sedimentary barite is present in several Marinoan cap carbonates (Deynoux and Trompette, 1981; Kennedy, 1996; Hoffman and Schrag, 2002; Jiang and others, 2006; Shields and others, 2007). Barium is also soluble in anoxic water and precipitates as barite in the presence of sulfate. An atmospheric sulfur isotope signal in the Marinoan barites suggests the sulfur was derived from shallow water as sulfate rather than deep waters as sulfide (Bao and others, 2008). Moreover, FeP:FeHR < 0.8 in Ediacaran shales indicates that ferruginous, and not euxinic conditions, prevailed after the Marinoan glaciation (Canfield and others, 2008; Shen and others, 2008). Thus, like the *ca.* 716.5 Ma Sturtian ocean, the *ca.* 635 Ma Marinoan ocean appears to have been anoxic but not euxinic, yet one produced iron formation and the other produced barite. This difference could be due to: 1) different S:Fe flux into the ocean at the onset of the two glaciations; 2) an increase in atmospheric oxygen and sulfate availability between the two glaciations; 3) different degrees of ice cover, primary productivity, and organic carbon availability for BSR during the two glaciations; and 4) different durations of the two glaciations with a longer Sturtian glaciation driving decreased S:Fe ratios in the ocean. Future geochemical and geochronological studies will help distinguish between these models and lead towards an understanding of the origin of Cryogenian chemical sediments and the secular evolution of the environments that produced them.

CONCLUSIONS

Integrated geological mapping with chemo- and litho-stratigraphic studies in the PNG of Namibia and South Africa suggest that the Numees Formation is a Sturtian-age diamictite. With existing age constraints, this scenario is consistent with Neoproterozoic glacial records globally. Particularly, 1) the *ca.* 750 Ma age constraint on the Kaigas Formation is too old for a Sturtian glacial deposit; 2) the presence of microbial roll-up

structures, a characteristic $\delta^{13}C$ profile, and relatively low Sr isotopic ratios in the Bloeddrif cap limestone is consistent with its assignment as a Sturtian-age cap carbonate; and 3) the $\delta^{13}C$ profile, elevated Sr isotopic composition, and sedimentary structures of the Dreigratberg cap carbonate are characteristic of basal Ediacaran cap carbonates. The correlations presented herein suggest that recent tectonic models that claim the upper portion of the Hilda Subgroup and Numees Formation were deposited in a back-arc basin and the overlying Holgat Formation formed in a foredeep basin, are untenable. We suggest that the entire PNG was deposited along a rifted passive margin and that foredeep sedimentation began at the base of the Nama Group. The new correlations also suggest that the Jakkalsberg Member iron formation of the Numees diamictite is Sturtian in age. This leaves few, if any, possible Marinoan-aged iron formations.

ACKNOWLEDGMENTS

We thank Sarah Bahan, Alexandra Breus, Tom Benson, and Hess Yntema for help in the field. We thank Greg Eischeid and John Higgins for assistance with elemental and isotopic analyses. We thank Sam Bowring for use of MIT's Radiogenic Isotope Lab. We thank Tanja Bosak, Sara Pruss and the NSF for support in 2009 (EAR-0843358). We thank Paul Hoffman for suggesting beginning study of the Gariep belt at the Naskluft Camp section, for providing support (pre-2009) from NSF grant EAR-0417422, and for comments on the manuscript. We thank the Geological Survey of Namibia for assistance with logistics. We also thank Nick Beukes, Simon Wilde, and an anonymous reviewer for their comments. We acknowledge Alfred Kroner for his thesis mapping in the Gariep Belt, which has held up with time and paved the way for our study.

APPENDIX

Geochemical Methods

Over 1000 samples were collected for carbon and oxygen isotopic analyses. All samples were cut perpendicular to lamination, revealing internal textures. Between 5 and 20 mg of powder were micro-drilled from the individual laminations (where visible), avoiding veining, cleavage, and siliciclastic components. Subsequent isotopic analyses were performed on aliquots of this powder. Carbonate $\delta^{13}C$ and $\delta^{18}O$ isotopic data were acquired simultaneously on a VG Optima dual inlet mass spectrometer attached to a VG Isocarb preparation device (Micromass, Milford, MA) in the Harvard University Laboratory for Geochemical Oceanography. Approximately, 1-mg micro-drilled samples were reacted in a common, purified H_3PO_4 bath at 90°C. Evolved CO_2 was collected cryogenically and analyzed using an in-house reference gas. External error (1σ) from standards was better than $\pm$ 0.1 permil for both $\delta^{13}C$ and $\delta^{18}O$. Samples were calibrated to VPDB (Vienna Pee-Dee Belemnite) using the Cararra marble standard. The memory effect potentially resulting from the common acid-bath system was minimized by increasing the reaction time for dolomite samples. Memory effect is estimated at <0.1 permil based on variability of standards run after dolomite samples. Carbon ($\delta^{13}C$) and oxygen ($\delta^{18}O$) isotopic results are reported in permil notation of $^{13}C/^{12}C$ and $^{18}O/^{16}O$, respectively, relative to the standard VPDB.

All $^{87}Sr/^{86}Sr$ data were acquired at the MIT Radiogenic Isotope Laboratory. Sample preparation methods are based on Gao and others (1996) and Bailey and others (2000). Approximately 10 mg of each powdered carbonate sample was first leached sequentially 3 to 5 times for 15 to 45 minutes in an ultrasonic bath, in 1.0 mL of 0.2 M ammonium acetate, to remove loosely bound Sr cations. The remaining solid was then washed 3 times in an ultrasonic bath with 1.0 mL of ultrapure water, to remove excess ammonium and suspended clays. Carbonate was reacted for 5 min. with 1.0 mL 1.4 M acetic acid and insoluble residue was removed by centrifuging. Sr was isolated via standard chromatographic techniques using 50 μL columns of EIChroM SR-spec resin. Samples were analyzed by thermal ionization mass spectrometry (TIMS) on a GV IsoProbe T in dynamic mode, with target intensity of 3V ^{88}Sr. All data were corrected to $^{86}Sr/^{88}Sr = 0.1194$ for internal mass bias. Each analysis represents a minimum of 60 ratio measurements, with internal precision of better than 0.001 percent ($1\text{-}\sigma$). Analyses were referenced against NBS SRM 987 (0.710250), with a long-term average of 0.710240 and $2\text{-}\sigma$ external precision of 0.000014 ($n > 100$). Data were not corrected for the slight low bias of measured values compared with the expected value of NBS 987.

TABLE A1

Carbon and oxygen isotope data

Section	Height (m)	$\delta^{13}C$	$\delta^{18}O$	Map Unit
Base of F539 at: S 27°51'55", E 16°53'30"				**Namaskluft Camp**
F539	0.2	-0.73	-9.46	Dreigratberg
F539	1.0	-1.05	-16.06	Dreigratberg
F539	2.0	-1.56	-15.19	Dreigratberg
F539	3.4	-3.81	-15.01	Dreigratberg
F539	4.8	-3.62	-14.64	Dreigratberg
F539	6.3	-3.85	-14.16	Dreigratberg
F539	8.3	-3.69	-13.83	Dreigratberg
F539	11.8	-3.59	-12.67	Dreigratberg
F539	14.0	-3.34	-11.69	Dreigratberg
F539	15.6	-3.72	-12.32	Dreigratberg
F539	17.3	-3.67	-12.88	Dreigratberg
F539	19.0	-3.62	-12.96	Dreigratberg
F539	21.1	-3.84	-13.38	Dreigratberg
F539	23.0	-3.75	-13.08	Dreigratberg
F539	24.0	-3.60	-13.24	Dreigratberg
F539	26.0	-3.47	-11.93	Dreigratberg
F539	27.2	-3.53	-12.78	Dreigratberg
F539	27.7	-3.12	-10.48	Dreigratberg
F539	29.2	-3.19	-10.14	Dreigratberg
F539	30.5	-2.97	-10.16	Dreigratberg
Base of F547 at: S 27°51'05", E 16°53'30"				**Namaskluft Camp**
F547	0.9	-2.30	-9.79	Dreigratberg
F547	1.6	-2.70	-10.40	Dreigratberg
F547	2.7	-2.70	-9.29	Dreigratberg
F547	5.1	-2.70	-8.89	Dreigratberg
F547	6.7	-2.90	-6.92	Dreigratberg
F547	8.0	-2.92	-7.06	Dreigratberg
F547	11.5	-2.78	-6.94	Dreigratberg
F547	13.3	-2.57	-7.04	Dreigratberg
F547	15.2	-2.59	-7.92	Dreigratberg
F547	16.6	-2.59	-7.10	Dreigratberg
F547	19.0	-2.63	-6.87	Dreigratberg
F547	21.0	-2.73	-7.03	Dreigratberg
F547	23.2	-2.65	-6.64	Dreigratberg
F547	24.8	-2.62	-6.71	Dreigratberg
F547	26.9	-2.49	-6.69	Dreigratberg
F547	29.4	-2.86	-7.74	Dreigratberg
F547	31.8	-3.02	-7.70	Dreigratberg
F547	34.0	-3.03	-7.74	Dreigratberg
F547 at: S 27°51'05", E 16°53'30"				**Namaskluft Camp**
F547	38.2	-3.05	-7.21	Dreigratberg
F547	39.3	-3.65	-7.14	Dreigratberg
F547	46.7	-4.27	-9.05	Dreigratberg
F547	52.0	-5.10	-10.60	Dreigratberg
F547	72.5	-5.55	-13.21	Dreigratberg
F547	82.3	-5.66	-13.06	Dreigratberg
Base of C511 at: S 27°52'00", E 16°52'35"				**Namaskluft Camp**
C511	15	-3.13	-9.41	Bloeddrif
C511	17.4	-1.54	-8.03	Bloeddrif
C511	20.9	-3.14	-13.98	Bloeddrif
C511	22.2	-2.68	-13.64	Bloeddrif
C511	24.9	-3.24	-11.16	Bloeddrif
C511	27.7	-4.16	-10.24	Bloeddrif
C511	29	-2.60	-6.39	Bloeddrif
C511	31.6	-3.39	-5.19	Bloeddrif
C511	32.7	-0.89	-3.72	Bloeddrif
C511	33.4	-1.69	-7.34	Bloeddrif
C511	35.5	-2.87	-12.29	Bloeddrif
C511	38	-2.61	-12.51	Bloeddrif
C511	40	-2.73	-9.37	Bloeddrif
C511	41	0.15	-0.65	Bloeddrif
C511	44.7	-1.53	-8.69	Bloeddrif
C511	48.2	-2.23	-12.17	Bloeddrif
C511	49.8	-2.56	-5.82	Bloeddrif
C511	52.4	-1.61	-10.43	Bloeddrif
C511	55.6	-2.25	-13.12	Bloeddrif
C511	60	-1.72	-11.22	Bloeddrif
C511	65.7	-1.70	-12.09	Bloeddrif
C511	70.5	-1.53	-12.93	Bloeddrif
C511	77.5	-1.63	-12.73	Bloeddrif
C511	80	-1.13	-5.84	Bloeddrif
C511	83.9	-1.67	-13.55	Bloeddrif
C511	91.8	-1.76	-14.07	Bloeddrif
C511	98.8	-1.79	-14.67	Bloeddrif
C511	104.3	-1.94	-14.10	Bloeddrif
C511	123.7	-2.82	-14.74	Bloeddrif
C511	128.3	-2.59	-11.40	Bloeddrif
C511	141	-2.17	-15.96	Bloeddrif
C511	158.4	-2.16	-14.20	Bloeddrif
C511 at: S 27°52'00", E 16°52'35"				**Namaskluft Camp**
C511	165	-1.77	-14.14	Bloeddrif
C511	173.4	-1.50	-14.35	Bloeddrif
C511	185	-1.70	-14.59	Bloeddrif
C511	276.9	-2.55	-16.54	Wallekraal
C511	304.2	-1.68	-16.96	Wallekraal
C511	325.2	-3.08	-17.14	Wallekraal
C511	399.3	-2.22	-17.04	Wallekraal
C511	420	-1.41	-16.31	Wallekraal
C511	453.2	-2.31	-14.13	Wallekraal
Base of F801 at: S 27°51'13", E 16°52'32"				**Namaskluft Camp**
F801	23.5	-8.59	-17.27	Numees clast
F801	31.5	-6.66	-17.50	Bloeddrif
F801	32.3	-4.22	-16.60	Bloeddrif
F801	33.2	-3.58	-15.82	Bloeddrif
F801	33.9	-3.76	-15.53	Bloeddrif
F801	35.0	-2.34	-10.68	Bloeddrif
F801	36.0	-2.46	-12.62	Bloeddrif
F801	37.0	-3.29	-14.59	Bloeddrif
F801	38.0	-2.73	-13.09	Bloeddrif
F801	38.7	-2.24	-11.72	Bloeddrif
F801	39.5	-2.36	-12.68	Bloeddrif
F801	41.0	-0.52	-0.82	Bloeddrif
F801	42.5	-3.04	-12.05	Bloeddrif
F801	44.0	-3.30	-11.26	Bloeddrif
F801	44.1	-2.77	-12.96	Bloeddrif
F801	45.0	-3.26	-10.62	Bloeddrif
F801	46.0	-3.08	-11.03	Bloeddrif
F801	47.3	-3.56	-12.63	Bloeddrif
F801	48.0	-3.25	-10.13	Bloeddrif
F801	49.4	-2.76	-10.45	Bloeddrif
F801	50.7	-2.80	-10.62	Bloeddrif
F801	51.8	-2.82	-10.33	Bloeddrif
F801	54.0	-2.40	-11.53	Bloeddrif
F801	54.7	-2.79	-12.92	Bloeddrif
F801	57.0	-1.41	-10.89	Bloeddrif
F801	59.0	-2.33	-13.39	Bloeddrif
F801	60.0	-1.84	-11.17	Bloeddrif
F801	65.0	-2.22	-13.51	Bloeddrif
F801	66.0	-2.24	-12.88	Bloeddrif

TABLE A1
(continued)

Section	Height (m)	$\delta^{13}C$	$\delta^{18}O$	Map Unit
F801 at: S 27°51'13", E 16°52'32"				**Namaskluft Camp**
F801	69.0	-0.20	-5.29	Bloeddrif
F801	71.0	1.33	2.13	Bloeddrif
F801	76.5	-0.50	-4.02	Bloeddrif
F801	78.0	-1.99	-13.88	Bloeddrif
F801	80.0	-1.96	-14.02	Bloeddrif
F801	82.0	-1.98	-14.49	Bloeddrif
F801	84.0	-2.02	-14.34	Bloeddrif
F801	91.0	-1.95	-14.12	Bloeddrif
F801	92.0	-2.01	-14.63	Bloeddrif
F801	98.8	-1.74	-14.46	Bloeddrif
F801	101.0	-1.35	-12.13	Bloeddrif
F801	104.8	-1.70	-14.44	Bloeddrif
Base of F804 at: S 28°38'39", E 17°05'33"				**Kaigas River**
F804	4.0	-0.04	-10.21	Dreigratberg
F804	4.5	-1.53	-11.78	Dreigratberg
F804	5.0	-2.14	-12.49	Dreigratberg
F804	5.6	-2.25	-11.11	Dreigratberg
F804	7.1	-1.51	-7.15	Dreigratberg
F804	8.0	-2.07	-7.82	Dreigratberg
F804	9.0	-2.22	-7.31	Dreigratberg
F804	9.9	-2.43	-6.66	Dreigratberg
F804	11.0	-2.36	-7.41	Dreigratberg
F804	12.0	-1.67	-6.45	Dreigratberg
F804	13.0	-2.40	-6.64	Dreigratberg
F804	14.3	-0.57	-5.83	Dreigratberg
F804	16.0	-0.35	-6.07	Dreigratberg
F804	17.0	-0.21	-5.21	Dreigratberg
F804	18.0	-0.35	-5.35	Dreigratberg
F804	19.0	-0.16	-5.78	Dreigratberg
F804	20.2	-0.79	-5.67	Dreigratberg
F804	21.0	-1.76	-4.75	Dreigratberg
F804	21.5	-0.63	-5.58	Dreigratberg
F804	22.4	-0.47	-5.89	Dreigratberg
F804	23.5	-0.77	-5.82	Dreigratberg
F804	24.3	-4.23	-4.22	Dreigratberg
F804	25.0	-0.57	-6.01	Dreigratberg
F804	26.0	-0.47	-6.11	Dreigratberg
F804	27.0	-0.98	-5.88	Dreigratberg
F804	27.9	-1.06	-6.24	Dreigratberg

Section	Height (m)	$\delta^{13}C$	$\delta^{18}O$	Map Unit
F804 at: S 28°38'39", E 17°05'33"				**Kaigas River**
F804	29.0	-0.82	-5.71	Dreigratberg
F804	30.0	-0.59	-5.59	Dreigratberg
F804	31.0	-0.66	-6.27	Dreigratberg
F804	32.0	-0.27	-5.97	Dreigratberg
F804	33.0	0.04	-6.02	Dreigratberg
F804	34.0	0.08	-6.62	Dreigratberg
F804	29.0	-0.82	-5.71	Dreigratberg
F804	34.8	0.17	-6.35	Dreigratberg
F804	36.0	0.03	-6.09	Dreigratberg
F804	37.0	0.12	-6.42	Dreigratberg
F804	37.8	0.01	-6.27	Dreigratberg
F804	38.4	-0.03	-6.60	Dreigratberg
F804	41.5	-1.44	-3.86	Dreigratberg
F804	43.0	-0.21	-6.36	Dreigratberg
F804	45.0	-0.29	-5.76	Dreigratberg
Base of F805 at: S 28°39'32", E 17°06'33"				**Holgat River**
F805	76.0	-0.94	-10.11	lower Holgat
F805	80.0	0.14	-12.16	lower Holgat
F805	84.0	0.38	-3.45	lower Holgat
F805	88.0	0.56	-11.96	lower Holgat
F805	90.0	1.31	-13.86	lower Holgat
F805	92.0	-0.28	-10.95	lower Holgat
F805	102.0	1.88	-2.70	lower Holgat
F805	106.0	1.31	-12.63	lower Holgat
F805	110.0	1.82	-3.56	lower Holgat
F805	116.0	1.70	-11.06	lower Holgat
F805	124.0	1.19	-9.45	lower Holgat
F805	129.0	1.21	-12.67	lower Holgat
F805	140.5	4.11	-14.67	lower Holgat
F805	150.0	4.00	-11.03	lower Holgat
F805	153.0	4.53	-14.49	lower Holgat
F805	158.0	5.49	-14.61	lower Holgat
F805	163.0	-0.57	-15.25	lower Holgat
F805	170.0	6.04	-15.11	lower Holgat
F805	172.0	6.83	-14.31	lower Holgat
F805	175.0	6.77	-12.78	lower Holgat
F805	177.0	7.09	-14.57	lower Holgat
F805	179.0	6.84	-13.74	lower Holgat
F805	184.0	7.21	-13.49	lower Holgat

Section	Height (m)	$\delta^{13}C$	$\delta^{18}O$	Map Unit
F805 at: S 28°39'32", E 17°06'33"				**Holgat River**
F805	190.0	4.71	-6.13	lower Holgat
F805	194.0	3.89	-13.55	lower Holgat
Base of F806 at : S28 39'11.0", E17 06'32.2"				**Kaigas River**
F806	0.3	-5.45	-15.12	Bloeddrif
F806	0.9	-2.90	-15.97	Bloeddrif
F806	1.7	-4.22	-13.02	Bloeddrif
F806	2.2	-2.18	-14.82	Bloeddrif
F806	2.6	-2.24	-14.99	Bloeddrif
F806	3	-2.16	-15.25	Bloeddrif
F806	3.5	-1.84	-14.56	Bloeddrif
F806	4	-2.78	-11.69	Bloeddrif
F806	4.6	-1.74	-15.67	Bloeddrif
F806	5	-1.56	-10.80	Bloeddrif
F806	6.1	-1.22	-14.36	Bloeddrif
F806	6.5	-1.05	-13.71	Bloeddrif
F806	7.1	-1.39	-14.21	Bloeddrif
F806	7.5	-3.26	-2.38	Bloeddrif
F806	8	-3.86	-7.85	Bloeddrif
F806	9.5	-1.43	-12.73	Bloeddrif
F806	10	-1.52	-14.55	Bloeddrif
F806	10.5	-1.31	-14.91	Bloeddrif
F806	11	-1.20	-12.94	Bloeddrif
Base of F807 at: S 28°22'52", E 16°50'06"				**Bloeddrif**
F807	0.5	-1.57	-15.01	Bloeddrif
F807	1.1	-3.77	-8.66	Bloeddrif
F807	2	-3.50	-6.43	Bloeddrif
F807	3.2	-2.53	-5.17	Bloeddrif
F807	4.7	-2.96	-4.60	Bloeddrif
F807	0.5	-1.57	-15.01	Bloeddrif
F807	6	-4.00	-4.18	Bloeddrif
F807	7	-4.33	-4.03	Bloeddrif
F807	8	-4.61	-4.65	Bloeddrif
F807	10	-4.81	-4.28	Bloeddrif
F807	11	-1.18	-4.12	Bloeddrif
Base of F808 at: S 28°19'25", E 16°55'11"				**Annisfontein**
F808	0	-6.43	-15.60	Bloeddrif
F808	0.5	-5.98	-15.29	Bloeddrif
F808	1	-6.92	-15.80	Bloeddrif
F808	1.5	-1.62	-15.85	Bloeddrif

TABLE A1
(continued)

Section	Height (m)	$\delta^{13}C$	$\delta^{18}O$	Map Unit
F808 at: S 28°19'25", E 16°55'11"				**Annisfontein**
F808	2	-5.44	-13.03	Bloeddrif
F808	2.5	-6.08	-14.53	Bloeddrif
F808	3	-5.22	-15.64	Bloeddrif
F808	3.3	-6.41	-12.40	Bloeddrif
F808	27.5	-6.29	-12.02	Bloeddrif
F808	48	-3.49	-11.10	Bloeddrif
F808	50	-3.72	-15.76	Bloeddrif
F808	54.5	-3.06	-13.83	Bloeddrif
F808	56	-1.74	-14.00	Bloeddrif
F808	58	-1.84	-14.20	Bloeddrif
F808	60	-1.88	-13.02	Bloeddrif
F808	62	-1.54	-13.72	Bloeddrif
F808	54.5	-3.06	-13.83	Bloeddrif
Base of F810 at: S 28°19', E 16°59'				**Numees Mine**
F810	1	1.71	-9.12	Wallekraal
F810	2.1	1.38	-10.84	Wallekraal
F810	3	1.59	-13.34	Wallekraal
F810	8	2.46	0.63	Wallekraal
F810	60	4.25	-6.85	Dabbie River
F810	69	4.05	-5.83	Dabbie River
F810	71	3.89	-5.84	Dabbie River
F810	78	4.90	-6.32	Dabbie River
F810	85	4.89	-5.69	Dabbie River
F810	89	3.70	-4.92	Dabbie River
F810	93	4.37	-5.54	Dabbie River
F810	107	4.46	-7.15	Dabbie River
F810	116	4.91	-6.58	Dabbie River
F810	128	4.01	-5.17	Dabbie River
F810	136	4.65	-7.98	Dabbie River
F810	137	5.48	-9.68	Dabbie River
F810	144	3.81	-8.62	Dabbie River
F810	148	4.05	-11.21	Dabbie River
Base of F811 at: S 28°18', E 16°59'				**Numees Mine**
F811	0.0	-5.95	-13.48	Bloeddrif
F811	1.0	-4.26	-17.14	Bloeddrif
F811	3.0	-3.90	-17.02	Bloeddrif
F811	5.0	-3.11	-14.98	Bloeddrif
F811	7.0	-2.88	-16.04	Bloeddrif
F811	13.0	-0.55	-6.55	Bloeddrif
F811 at: S 28°18', E 16°59'				**Numees Mine**
F811	16.0	-2.32	-11.94	Bloeddrif
F811	20.0	-3.52	-9.17	Bloeddrif
F811	24.0	-2.00	-10.73	Bloeddrif
F811	26.2	-1.90	-5.03	Bloeddrif
F811	28.0	-2.19	-8.13	Bloeddrif
F811	32.0	-1.92	-4.62	Bloeddrif
F811	36.0	-2.53	-13.94	Bloeddrif
F811	41.0	-2.69	-12.85	Bloeddrif
Base of F816 at: S 28°06'23", E 16°52'53"				**Dreigratberg**
F816	0.5	-3.86	-14.70	Bloeddrif
F816	1.1	-5.98	-15.71	Bloeddrif
F816	1.8	-4.83	-15.18	Bloeddrif
F816	4.0	-4.70	-10.77	Bloeddrif
F816	4.8	-3.81	-6.21	Bloeddrif
F816	6.0	-3.93	-10.33	Bloeddrif
F816	8.1	-4.54	-12.09	Bloeddrif
F816	18.5	0.01	-14.43	lower Holgat
F816	20.0	0.51	-14.45	lower Holgat
F816	22.0	1.16	-13.89	lower Holgat
F816	27.0	0.45	-13.70	lower Holgat
F816	38.5	0.79	-13.57	lower Holgat
F816	50.0	1.89	-12.83	lower Holgat
F816	54.0	-1.00	-14.05	lower Holgat
F816	58.4	-3.42	-12.37	lower Holgat
F816	60.0	-4.63	-6.75	lower Holgat
F816	76.0	-9.00	-13.56	lower Holgat
F816	88.5	-1.62	-10.71	Dreigratberg
F816	90.0	-2.30	-9.08	Dreigratberg
F816	97.0	-3.57	-10.35	Dreigratberg
F816	100.5	-3.88	-9.47	Dreigratberg
F816	102.0	-3.90	-8.90	Dreigratberg
F816	114.0	-3.27	-9.67	Dreigratberg
F816	115.0	-3.12	-10.21	Dreigratberg
F816	118.0	-2.89	-10.36	Dreigratberg
F816	119.4	-2.07	-9.25	Dreigratberg
F816	129.0	-0.69	-9.24	Dreigratberg
F816	137.0	-2.01	-10.66	Dreigratberg
F816	148.0	-2.27	-11.73	Dreigratberg
F816	156.0	-2.29	-11.25	Dreigratberg
F816 at: S 28°06'23", E 16°52'53"				**Dreigratberg**
F816	170.0	0.86	-7.28	upper Holgat
F816	178.0	0.79	-6.47	upper Holgat
F816	182.0	3.05	-3.57	upper Holgat
F816	186.0	1.46	-4.28	upper Holgat
F816	190.0	1.56	-4.01	upper Holgat
F816	198.0	0.31	-6.44	upper Holgat
F816	199.5	0.36	-7.08	upper Holgat
F816	201.0	0.18	-6.86	upper Holgat
F816	203.0	0.80	-6.31	upper Holgat
F816	215.0	2.03	-2.90	upper Holgat
F816	219.0	2.41	-3.63	upper Holgat
F816	224.0	2.98	-2.10	upper Holgat
F816	229.0	0.72	-4.05	upper Holgat
F816	231.5	0.27	-4.05	upper Holgat
F816	234.0	2.41	-2.28	upper Holgat
F816	236.0	3.65	-2.05	upper Holgat
F816	237.0	3.78	-2.30	upper Holgat
F816	238.0	4.14	-2.18	upper Holgat
F816	241.0	4.91	-0.99	upper Holgat
F816	256.0	4.02	-4.79	upper Holgat
F816	259.0	2.93	-5.02	upper Holgat
F816	266.0	0.33	-7.56	upper Holgat
F816	267.0	0.33	-7.82	upper Holgat
F816	285.0	4.12	-3.65	upper Holgat
F816	299.0	0.26	-5.55	upper Holgat
F816	350.0	-0.06	-4.44	upper Holgat
F816	353.0	0.93	-2.02	upper Holgat
F816	357.0	2.01	-3.63	upper Holgat
F816	359.0	2.04	-1.28	upper Holgat
F816	361.0	2.36	-0.92	upper Holgat
F816	363.0	3.42	-1.77	upper Holgat
F816	365.0	3.15	-1.79	upper Holgat
F816	367.0	2.31	-5.09	upper Holgat
F816	371.0	2.72	-4.10	upper Holgat
F816	375.0	3.75	-3.27	upper Holgat
F816	379.0	3.50	-1.93	upper Holgat
F816	383.0	1.77	-3.15	upper Holgat
Base of F817 at: S 27°51'53", E 16°53'57"				**Namaskluft Camp**
F817	0.5	1.65	-1.99	Dreigratberg

TABLE A1
(continued)

Section	Height (m)	$\delta^{13}C$	$\delta^{18}O$	Map Unit
F817 at: S 27°51'53", E 16°53'57"				**Namaskluft Camp**
F817	1.0	-2.52	-15.12	Dreigratberg
F817	1.7	-3.21	-16.22	Dreigratberg
F817	2.1	-3.76	-13.82	Dreigratberg
F817	2.3	-3.93	-15.48	Dreigratberg
F817	2.9	-3.27	-17.32	Dreigratberg
F817	4.0	-3.19	-19.13	Dreigratberg
F817	5.5	-3.20	-15.26	Dreigratberg
F817	5.8	-3.69	-15.47	Dreigratberg
F817	6.2	-3.62	-15.50	Dreigratberg
F817	6.8	-3.74	-15.37	Dreigratberg
F817	7.5	-3.65	-15.96	Dreigratberg
F817	8.0	-3.61	-15.59	Dreigratberg
F817	8.5	-3.53	-14.78	Dreigratberg
F817	9.0	-3.57	-15.14	Dreigratberg
F817	9.5	-3.54	-15.54	Dreigratberg
F817	10.0	-3.52	-14.73	Dreigratberg
F817	10.7	-3.57	-14.81	Dreigratberg
F817	11.3	-3.49	-14.53	Dreigratberg
F817	12.0	-3.37	-14.43	Dreigratberg
F817	12.3	-3.43	-14.07	Dreigratberg
F817	13.0	-3.18	-13.22	Dreigratberg
F817	13.7	-2.93	-12.38	Dreigratberg
F817	14.1	-2.72	-11.57	Dreigratberg
F817	15.1	-2.78	-11.74	Dreigratberg
F817	16.0	-2.73	-9.86	Dreigratberg
F817	17.0	-2.78	-9.37	Dreigratberg
F817	18.0	-2.80	-8.45	Dreigratberg
F817	19.0	-2.96	-8.91	Dreigratberg
F817	21.0	-2.90	-9.38	Dreigratberg
F817	23.0	-2.86	-9.17	Dreigratberg
F817	25.0	-2.84	-8.48	Dreigratberg
F817	45.0	-3.63	-10.81	Dreigratberg
F817	46.3	-3.65	-11.39	Dreigratberg
F817	64.0	1.65	-1.99	Dreigratberg
F817	66.0	-4.25	-12.57	Dreigratberg
F817	69.0	-4.64	-13.77	Dreigratberg
F817	71.0	-4.92	-14.55	Dreigratberg
F817	83.0	-4.19	-12.15	Dreigratberg
F817	101.0	-4.58	-13.61	Dreigratberg
F817 at: S 27°51'53", E 16°53'57"				**Namaskluft Camp**
F817	113.0	-5.35	-14.28	Dreigratberg
F817	148.0	-5.28	-14.68	Dreigratberg
F817	149.0	-5.56	-14.82	Dreigratberg
F817	150.0	-5.49	-15.20	Dreigratberg
F817	166.0	-5.54	-15.13	Dreigratberg
F817	175.0	-5.02	-17.90	Dreigratberg
F817	200.0	-5.50	-14.72	Dreigratberg
F817	217.0	-5.46	-14.38	Dreigratberg
F817	218.0	-5.49	-14.25	Dreigratberg
F817	232.0	-5.55	-14.03	Dreigratberg
F817	240.0	-5.71	-11.62	Dreigratberg
F817	241.0	-5.36	-13.76	Dreigratberg
F817	244.0	-5.44	-13.77	Dreigratberg
F817	248.0	-3.62	-9.69	Dreigratberg
F817	255.0	-4.77	-12.43	Dreigratberg
F817	260.0	-5.61	-11.60	Dreigratberg
F817	261.0	-5.37	-13.75	Dreigratberg
F817	268.0	-5.45	-13.72	Dreigratberg
F817	278.0	-5.39	-13.45	Dreigratberg
F817	283.0	-5.32	-13.58	Dreigratberg
F817	284.0	-5.34	-13.75	Dreigratberg
F817	290.0	-5.34	-13.56	Dreigratberg
F817	292.0	-5.50	-13.79	Dreigratberg
F817	296.0	-5.19	-13.51	Dreigratberg
F817	311.0	-5.48	-13.32	Dreigratberg
F817	312.0	-5.48	-13.48	Dreigratberg
F817	314.0	-5.12	-14.30	Dreigratberg
F817	318.0	-5.61	-13.75	Dreigratberg
F817	320.0	-5.56	-12.58	Dreigratberg
F817	321.0	-5.46	-13.37	Dreigratberg
F817	322.0	-5.36	-13.34	Dreigratberg
F817	323.5	-5.54	-12.76	Dreigratberg
F817	325.0	-5.30	-12.69	Dreigratberg
F817	327.0	-5.30	-12.29	Dreigratberg
F817	329.0	-5.15	-14.44	Dreigratberg
F817	331.0	-5.11	-10.92	Dreigratberg
F817	334.0	-5.22	-14.56	Dreigratberg
F817	336.0	-5.03	-11.45	Dreigratberg
Base of F818 at: S 28°00'29", E 16°51'19				**Namaskluft Farm**
F818	0.2	-0.02	-7.15	Dreigratberg
F818	0.7	-1.13	-7.33	Dreigratberg
F818	1.0	-1.37	-7.54	Dreigratberg
F818	1.5	-1.95	-7.74	Dreigratberg
F818	2.0	-2.14	-7.83	Dreigratberg
F818	2.5	-2.23	-7.87	Dreigratberg
F818	3.0	-2.06	-7.37	Dreigratberg
F818	5.0	-2.19	-8.00	Dreigratberg
F818	7.0	-1.96	-7.63	Dreigratberg
F818	9.0	-2.13	-6.91	Dreigratberg
F818	11.0	-1.83	-7.05	Dreigratberg
F818	13.0	-1.83	-7.22	Dreigratberg
F818	15.0	-1.91	-7.37	Dreigratberg
F818	17.0	-1.85	-7.06	Dreigratberg
F818	19.0	-1.87	-7.05	Dreigratberg
F818	21.0	-2.16	-7.12	Dreigratberg
F818	23.0	-1.82	-7.63	Dreigratberg
F818	25.0	-1.83	-6.78	Dreigratberg
F818	27.0	-1.84	-7.04	Dreigratberg
F818	29.0	-2.04	-7.04	Dreigratberg
F818	31.0	-1.90	-7.06	Dreigratberg
F818	33.0	-2.08	-6.66	Dreigratberg
F818	35.0	-1.93	-6.76	Dreigratberg
F818	37.0	-2.34	-7.02	Dreigratberg
F818	39.0	-2.90	-6.85	Dreigratberg
Base of F819 at: S 28°00'47", E 16°51'32"				**Namaskluft Farm**
F819	15.0	-2.07	-15.46	Bloeddrif
F819	15.5	-1.74	-17.04	Bloeddrif
F819	16.0	-1.03	-15.86	Bloeddrif
F819	16.5	-1.03	-16.58	Bloeddrif
F819	17.0	2.21	-14.97	Bloeddrif
F819	17.5	2.46	-12.80	Bloeddrif
F819	18.5	-1.38	-15.71	Bloeddrif
F819	20.0	1.65	-11.81	lower Holgat
F819	21.0	-0.48	-14.25	lower Holgat
F819	22.0	0.95	-13.02	lower Holgat
F819	23.0	1.38	-12.99	lower Holgat
F819	24.0	1.34	-12.19	lower Holgat
F819	24.5	2.27	-11.63	lower Holgat

TABLE A1
(continued)

Section	Height (m)	$\delta^{13}C$	$\delta^{18}O$	Map Unit
F819 at: S 28°00'47", E 16°51'32"				**Namaskluft Farm**
F819	33.0	2.70	-8.79	lower Holgat
F819	37.0	2.68	-8.00	lower Holgat
F819	40.0	0.22	-8.23	lower Holgat
F819	42.0	0.66	-7.84	lower Holgat
F819	44.0	0.14	-7.34	lower Holgat
F819	48.0	2.28	-9.45	lower Holgat
F819	50.0	2.35	-9.48	lower Holgat
F819	52.0	0.95	-9.35	lower Holgat
F819	53.5	7.30	-4.25	lower Holgat
F819	59.0	6.39	-5.63	lower Holgat
F819	64.0	7.45	-5.00	lower Holgat
F819	70.0	5.85	-7.82	lower Holgat
F819	77.0	4.36	-4.96	lower Holgat
F819	81.0	6.39	-3.49	lower Holgat
F819	86.0	3.41	-6.47	lower Holgat
F819	107.0	3.58	-7.23	lower Holgat
F819	111.0	5.94	-6.62	lower Holgat
F819	115.0	7.86	-4.95	lower Holgat
F819	125.0	7.33	-6.03	lower Holgat
F819	133.5	6.86	-7.12	lower Holgat
F819	134.5	6.27	-10.90	lower Holgat
F819	146.0	6.63	-8.81	lower Holgat
F819	208.0	-0.13	-12.27	lower Holgat
F819	219.0	-2.49	-11.86	lower Holgat
F819	226.0	2.32	-8.35	Dabie River
F819	227.0	5.18	-6.06	Dabie River
F819	229.0	3.26	-6.90	Dabie River
F819	231.0	-0.56	-8.65	Dabie River
F819	233.0	-3.28	-6.68	Dabie River
F819	235.0	-2.72	-6.26	Dabie River
F819	238.0	-2.52	-7.30	Dabie River
F819	242.0	-1.41	-8.16	Dabie River
F819	244.0	-0.42	-8.05	Dabie River
F819	246.0	0.38	-8.10	Dabie River
F819	247.0	0.59	-7.60	Dabie River
F819	248.0	-0.73	-7.39	Dabie River
F819	249.0	-1.05	-6.84	Dabie River
F819	250.0	-1.39	-6.76	Dabie River
F819	251.0	-2.29	-7.16	Dabie River
F819 at: S 28°00'47", E 16°51'32"				**Namaskluft Farm**
F819	252.0	-1.77	-7.04	Dabie River
F819	253.0	-1.48	-6.91	Dabie River
F819	281.0	4.35	-3.27	Numees
F819	285.0	-0.26	-7.42	Dreigratberg
F819	285.5	-1.30	-7.51	Dreigratberg
F819	286.0	-2.32	-7.36	Dreigratberg
F819	286.5	-2.33	-7.59	Dreigratberg
F819	287.0	-2.03	-7.43	Dreigratberg
F819	287.5	-2.20	-7.33	Dreigratberg
F819	288.0	-2.15	-7.32	Dreigratberg
F819	289.0	-2.22	-7.83	Dreigratberg
F819	290.0	-2.09	-7.60	Dreigratberg
F819	291.0	-2.30	-7.06	Dreigratberg
F819	292.0	-2.51	-6.65	Dreigratberg
F819	293.0	-2.59	-6.81	Dreigratberg
F819	294.0	-2.27	-7.24	Dreigratberg
F819	295.0	-2.67	-6.76	Dreigratberg
Base of F820 at: S 28°00'47", E 16°51'32"				**Namaskluft Farm**
F820	249.0	-2.50	-5.20	Bloeddrif
F820	251.0	-3.02	-5.23	Bloeddrif
F820	252.0	-3.73	-5.82	Bloeddrif
F820	253.0	-3.48	-5.53	Bloeddrif
F820	254.0	-3.80	-4.01	Bloeddrif
F820	255.0	-4.03	-5.48	Bloeddrif
F820	257.0	-3.90	-6.06	Bloeddrif
F820	258.0	-3.39	-6.13	Bloeddrif
F820	259.0	-3.21	-7.00	Bloeddrif
F820	260.0	-3.13	-7.28	Bloeddrif
F820	261.0	-2.64	-7.70	Bloeddrif
F820	262.0	-2.64	-7.74	Bloeddrif
Base of F823 at: S 27°48'25", E 16°39'53"				**Trekpoort Farm**
F823	1	2.62	-15.08	Picklehaube
F823	2.6	0.89	-14.38	Picklehaube
F823	6	2.11	-15.47	Picklehaube
F823	52	-0.74	-13.06	Picklehaube
F823	88	3.64	-9.33	Picklehaube
F823	89	0.64	-13.43	Picklehaube
F823	91	2.46	-9.63	Picklehaube
F823	93	3.94	-5.88	Picklehaube
F823 at: S 27°48'25", E 16°39'53"				**Trekpoort Farm**
F823	95	0.17	-10.95	Picklehaube
F823	97	1.69	-9.63	Picklehaube
F823	127.5	-4.78	-13.41	Picklehaube
F823	128.5	-4.70	-11.61	Picklehaube
F823	131	-1.79	-14.03	Picklehaube
F823	143	-0.71	-12.26	Picklehaube
F823	208	-1.32	-7.93	Numees
Base of F824 at: S 27°45'15", E 16°38'24"				**Trekpoort Farm**
F824	1	0.59	-14.50	Hilda Sgp.
F824	14	4.08	-13.37	Hilda Sgp.
F824	18	5.79	-13.06	Hilda Sgp.
F824	19	4.01	-13.55	Hilda Sgp.
F824	20.5	4.75	-11.72	Hilda Sgp.
F824	21.5	4.95	-11.60	Hilda Sgp.
F824	23.5	5.88	-10.23	Hilda Sgp
F824	24.5	5.52	-10.33	Hilda Sgp.
F824	26	4.83	-9.99	Hilda Sgp.
F824	34	4.72	-10.66	Hilda Sgp.
F824	35.5	3.93	-12.37	Hilda Sgp.
F824	48.5	4.76	-10.21	Hilda Sgp.
F824	51	6.70	-10.46	Hilda Sgp.
F824	69	4.28	-7.82	Hilda Sgp.
F824	201.3	7.33	-13.44	Hilda Sgp.
F824	201.8	7.07	-14.70	Hilda Sgp.
F824	202.5	6.09	-13.11	Hilda Sgp.
F824	204.5	6.86	-13.89	Hilda Sgp.
F824	205.5	7.20	-13.56	Hilda Sgp.
F824	207.5	6.27	-14.84	Hilda Sgp.
Base of F826 at: S 27°48'24", E 16°53'15"				**Namaskluft Camp**
F826	39.0	-0.41	-11.06	Walekrall
F826	108.0	2.08	-8.21	lower Holgat
F826	115.0	2.95	-12.13	lower Holgat
F826	122.0	2.45	-11.31	lower Holgat
F826	138.0	1.88	-11.14	lower Holgat
F826	176.0	2.15	-11.30	lower Holgat
F826	180.0	2.44	-12.42	lower Holgat
F826	184.0	2.44	-11.74	lower Holgat
F826	190.0	2.68	-13.18	lower Holgat
F826	193.0	2.78	-11.18	lower Holgat

TABLE A1
(continued)

Section	Height (m)	$\delta^{13}C$	$\delta^{18}O$	Map Unit
F826 at: S 27°48'24", E 16°53'15"				**Namaskluft Camp**
F826	197.0	2.83	-10.54	lower Holgat
F826	203.0	2.40	-10.58	lower Holgat
F826	206.0	2.55	-11.33	lower Holgat
F826	210.0	2.54	-11.46	lower Holgat
F826	214.0	1.99	-11.12	lower Holgat
F826	218.0	2.17	-11.30	lower Holgat
F826	224.0	2.46	-9.97	lower Holgat
F826	229.0	2.51	-10.42	lower Holgat
F826	234.0	2.52	-10.51	lower Holgat
F826	238.0	2.34	-10.08	lower Holgat
F826	241.0	2.21	-9.83	lower Holgat
F826	251.0	2.44	-11.19	lower Holgat
F826	255.0	2.44	-11.04	lower Holgat
F826	259.0	2.86	-10.32	lower Holgat
F826	266.0	2.56	-9.73	lower Holgat
F826	270.0	2.85	-10.24	lower Holgat
F826	271.0	2.78	-10.88	lower Holgat
F826	272.0	2.22	-9.52	lower Holgat
Base of F827 at: S 27°48'24", E 16°53'15"				**Namaskluft Camp**
F827	2.0	2.25	-10.63	lower Holgat
F827	3.0	2.02	-10.67	lower Holgat
F827	4.0	2.21	-10.88	lower Holgat
F827	6.0	2.33	-10.56	lower Holgat
F827	8.0	2.16	-10.46	lower Holgat
F827	9.0	2.42	-10.01	lower Holgat
F827	10.0	2.39	-11.01	lower Holgat
F827	11.0	2.32	-11.36	lower Holgat
F827	12.0	2.33	-10.88	lower Holgat
F827	13.0	2.31	-10.67	lower Holgat
F827	14.0	1.86	-9.26	lower Holgat
F827	15.0	2.33	-10.69	lower Holgat
F827	16.0	2.38	-9.32	lower Holgat
F827	17.0	2.70	-8.70	lower Holgat
F827	18.0	2.42	-9.37	lower Holgat
F827	19.0	2.09	-9.68	lower Holgat
F827	20.0	2.25	-10.05	lower Holgat
F827	21.0	2.08	-11.12	lower Holgat
F827	24.5	1.70	-8.73	lower Holgat
F827	35.0	-2.17	-11.89	Dabie River
F827	36.6	-3.32	-10.92	Dabie River
F827 at: S 27°48'24", E 16°53'15"				**Namaskluft Camp**
F827	37.5	-4.36	-11.89	Dabie River
F827	38.5	-5.15	-11.26	Dabie River
F827	47.0	-0.26	-10.02	Nama
F827	47.5	-0.27	-6.93	Nama
Base of F911 at: S 28°00'29", E 16°51'19"				**Namaskluft Farm**
F911	0.0	-2.85	-7.20	Dreigratberg
F911	1.0	-2.98	-5.96	Dreigratberg
F911	2.0	-3.10	-5.87	Dreigratberg
F911	3.0	-3.03	-6.20	Dreigratberg
F911	4.6	-4.13	-6.53	Dreigratberg
F911	6.0	-4.47	-6.66	Dreigratberg
F911	7.0	-5.10	-8.54	Dreigratberg
F911	8.0	-4.53	-9.05	Dreigratberg
F911	10.0	-4.75	-8.72	Dreigratberg
F911	12.0	-4.76	-8.54	Dreigratberg
F911	14.0	-4.56	-9.48	Dreigratberg
F911	16.0	-4.53	-9.46	Dreigratberg
F911	18.0	-4.38	-9.26	Dreigratberg
F911	20.0	-4.37	-9.02	Dreigratberg
F911	23.0	-4.33	-9.00	Dreigratberg
F911	25.0	-3.61	-7.04	Dreigratberg
F911	29.0	-4.43	-9.09	Dreigratberg
F911	32.0	-4.32	-10.58	Dreigratberg
F911	34.0	-4.22	-10.15	Dreigratberg
F911	36.0	-3.96	-12.36	Dreigratberg
F911	56.0	2.60	-5.40	upper Holgat
F911	57.5	3.09	-5.04	upper Holgat
F911	59.0	3.45	-4.40	upper Holgat
F911	61.0	2.83	-6.06	upper Holgat
F911	64.0	2.11	-5.40	upper Holgat
F911	72.7	-3.41	-6.01	upper Holgat
F911	74.0	-2.90	-5.35	upper Holgat
F911	79.0	-4.41	-12.10	upper Holgat
F911	81.0	-2.50	-7.61	upper Holgat
Base of F912 at: S 28°06'23", E 16°52'53"				**Dreigratberg**
F912	12.0	-8.11	-12.52	lower Holgat
F912	14.0	-4.95	-12.66	lower Holgat
F912	15.0	-3.61	-9.97	lower Holgat
F912	16.0	-1.03	-11.85	lower Holgat
F912	17.0	-0.95	-11.60	lower Holgat
F912 at: S 28°06'23", E 16°52'53"				**Dreigratberg**
F912	24.9	-1.32	-11.21	Dreigratberg
F912	25.1	-1.29	-10.60	Dreigratberg
F912	25.3	-1.41	-10.17	Dreigratberg
F912	25.5	-1.53	-10.42	Dreigratberg
F912	25.8	-1.68	-10.24	Dreigratberg
F912	26.0	-1.60	-9.90	Dreigratberg
F912	26.2	-2.40	-9.00	Dreigratberg
F912	26.4	-3.02	-8.50	Dreigratberg
F912	26.6	-2.91	-9.23	Dreigratberg
F912	27.2	-2.91	-8.75	Dreigratberg
F912	28.0	-2.69	-9.02	Dreigratberg
F912	29.0	-2.68	-8.96	Dreigratberg
F912	34.0	-3.83	-11.59	Dreigratberg
F912	35.0	-3.85	-11.16	Dreigratberg
F912	36.0	-4.16	-10.86	Dreigratberg
F912	37.0	-4.16	-	Dreigratberg
F912	38.0	-4.03	-10.56	Dreigratberg
F912	39.0	-3.80	-9.70	Dreigratberg
F912	40.0	-4.13	-11.67	Dreigratberg
F912	46.0	-3.66	-10.36	Dreigratberg
F912	48.0	-3.37	-10.92	Dreigratberg
F912	50.0	-3.50	-11.59	Dreigratberg
F912	52.8	-2.90	-11.49	Dreigratberg
F912	57.1	-2.52	-11.92	Dreigratberg
Base of F916 at: S 28°40'10", E 17°01'30"				**Dreigratberg**.
F916	0.1	-1.95	-2.65	Bloeddrif
F916	0.3	-1.55	-9.93	Bloeddrif
F916	0.5	-0.68	-8.34	Bloeddrif
F916	0.7	-1.62	-10.99	Bloeddrif
F916	0.9	-0.33	-7.76	Bloeddrif
F916	1	-3.42	-13.29	Bloeddrif
F916	1.4	-1.88	-8.77	Bloeddrif
F916	1.8	-0.93	-7.91	Bloeddrif
F916	2.2	-2.31	-0.95	Bloeddrif
F916	6.6	3.89	-11.75	Lower Holgat
F916	40.1	-3.61	-10.80	Dreigratberg
F916	40.5	-2.37	-8.20	Dreigratberg
F916	41	-2.44	-9.82	Dreigratberg
F916	42	-3.14	-10.73	Dreigratberg
F916	43	-2.53	-9.24	Dreigratberg

Strontium concentrations from section F539 were determined by inductively coupled plasma optical emission spectroscopy (ICP-OES) on a Jobin-Yvon 46P in the Harvard University Laboratory for Geochemical Oceanography. Samples were prepared by dissolving ~6 mg of carbonate powder in ~6 ml of 2 percent nitric acid. SCP single element standards were used for element-specific instrumental calibration. External error (1-σ) was determined by repeat analyses and was less than 5 percent. Additional elemental analyses were performed commercially at Actlabs in Ancaster, Ontario, where 0.5 g samples were digested in Aqua Regia at 90°C in a microprocessor controlled digestion block for 2 hours. The solution was diluted and analyzed using a Perkin Elmer SCIEX ELAN ICP/MS.

References

Alchin, D. J., Frimmel, H. E., and Jacobs, L. E., 2005, Stratigraphic setting of the metalliferous Rosh Pinah Formation and the Spitzkop and Koivib Suites in the Pan-African Gariep Belt, southwestern Namibia: South African Journal of Geology, v. 108, p. 19–36, doi: 10.2113/108.1.19.

Alvarenga, C. J. S. de, and Trompette, R., 1992, Glacially influenced sedimentation in the later Proterozoic of the Paraguay belt (Mato Grosso, Brazil): Palaeogeography, Palaeoclimatology, Palaeoecology, v. 92, p. 85–105, doi: 10.1016/0031-0182(92)90136-S.

Alvarenga, C. J. S. de, Dardenne, M. A., Santos, R. V., Brod, E. R., Gioia, S. M. C. L., Sial, A. N., Dantas, E. L., and Ferreira, V. P., 2008, Isotope stratigraphy of Neoproterozoic cap carbonates in the Aras Group, Brazil: Gondwana Research, v. 13, p. 469–479, doi: 10.1016/j.gr.2007.05.004.

Asmerom, Y., Jacobsen, S. B., Knoll, A. H., Butterfield, N. J., and Swett, K., 1991, Strontium isotopic variations of Neoproterozoic seawater: Implications for crustal evolution: Geochimica et Cosmochimica Acta, v. 55, p. 2883–2894, doi: 10.1016/0016-7037(91)90453-C.

Badenhorst, F. P., 1988, The lithostratigraphy of the Chuos mixtite in part of the southern central zone of the Damara Orogen, South West Africa: Communications of the Geological Survey of Namibia, v. 4, p. 103–110.

Bailey, T. R., McArthur, J. M., Prince, H., and Thirlwall, M. F., 2000, Dissolution methods for strontium isotope stratigraphy: whole rock anlysis: Chemical Geology, v. 167, p. 313–319, doi: 10.1016/S0009-2541(99)00235-1.

Banner, J. L., and Hanson, G. N., 1990, Calculation of simultaneous isotopic and trace element variations during water-rock interaction with applications to carbonate diagenesis: Geochimica et Cosmochimica Acta, v. 54, p. 3123–3137, doi: 10.1016/0016-7037(90)90128-8.

Bao, H., Lyons, J. R., and Zhou, C., 2008, Triple oxygen isotope evidence for elevated CO_2 levels after a Neoproterozoic glaciation: Nature, v. 453, p. 504–506, doi: 10.1038/nature06959.

Basei, M. A. S., Frimmel, H. E., Nutman, A. P., Perciozzi, F., and Jacob, J., 2005, A connection between the Neoproterozoic Dom Feliciano (Brazil/Uruguay) and Gariep (Namibia/South Africa) orogenic belts—evidence from a reconnaissance provenance study: Precambrian Research, v. 139, p. 195–221, doi: 10.1016/j.precamres.2005.06.005.

Borg, G., Kärner, K., Buxton, M., Armstrong, R., and Van der Merwe, S. W., 2003, Geology of the Skorpion zinc deposit, southern Namibia: Economic Geology, v. 98, p. 749–771, doi: 10.2113/98.4.749.

Bowring, S. A., Grotzinger, J. P., Condon, D. J., Ramezani, J., Newall, M. J., and Allen, P. A., 2007, Geochronologic constraints on the chronostratigraphic framework of the Neoproterozoic Huqf Supergroup, Sultanate of Oman: American Journal of Science, v. 307, p. 1097–1145, doi: 10.2475/10.2007.01.

Brasier, M. D., Shields, G., Kuleshov, V. N., and Zhegallo, E. A., 1996, Integrated chemo- and biostratigraphic calibration of early animal evolution: Neoproterozoic–early Cambrian of southwest Mongolia: Geological Magazine, v. 133, p. 445–485, doi: 10.1017/S0016756800007603.

Calver, C. R., 1998, Isotope stratigraphy of the Neoproterozoic Togari Group, Tasmania: Australian Journal of Earth Sciences, v. 45, p. 865–874, doi: 10.1080/08120099808728441.

Canfield, D. E., 2004, The evolution of the Earth surface sulfur reservoir: American Journal of Science, v. 304, p. 839–861, doi: 10.2475/ajs.304.10.839.

Canfield, D. E., Poulton, S. W., Knoll, A. H., Narbonne, G. M., Ross, G., Goldberg, T., and Strauss, H., 2008, Ferruginous conditions dominated later Neoproterozoic deep-water chemistry: Science, v. 321, p. 949–952, doi: 10.1126/science.1154499.

Chumakov, N. M., 2007, Climates and climate zonality of the Vendian: geological evidence, *in* Vickers-Rich, P., and Komarower, P., editors, The Rise and Fall of the Ediacaran Biota: Geological Society, London, Special Publications, v. 286, p. 15–26, doi: 10.1144/SP286.2.

Clifford, T. N., 2008, The geology of the Neoproterozoic Swakop-Otavi transition zone in the Outjo District, northern Damara Orogen, Namibia: South African Journal of Geology, v. 111, p. 117–140, doi: 10.2113/gssajg.111.1.117.

Corsetti, F. A., and Grotzinger, J. P., 2005, Origin and significance of tube structures in Neoproterozoic post-glacial cap carbonates: Example from Noonday Dolomite, Death Valley, United States: Palaios, v. 20, p. 348–363, doi: 10.2110/palo.2003.p03-96.

Corsetti, F. A., and Kaufman, A. J., 2003, Stratigraphic investigations of carbon isotope anomalies and Neoproterozoic ice ages in Death Valley, California: Geological Society of America Bulletin, v. 115, p. 916–932, doi: 10.1130/B25066.1.

Davies, C. J., and Coward, M. P., 1982, The structural evolution of the Gariep Arc in southern Namibia (South-West Africa: Precambrian Research, v. 17, p. 173–198, doi: 10.1016/0301-9268(82)90023-7.

De Villiers, J., and Söhnge, P. G., 1959, The geology of the Richtersveld: Memoirs of the Geological Survey of South Africa, v. 48, p. 1–295.

Derry, L. A., Keto, L. S., Jacobsen, S. B., Knoll, A. H., and Swett, K., 1989, Sr isotopic variations in Upper Proterozoic carbonates from Svalbard and East Greenland: Geochmica et Cosmochimica Acta, v. 53, p. 2231–2339, doi: 10.1016/0016-7037(89)90355-4.

Deynoux, M., and Trompette, R., 1981, Late Precambrian tillites of the Taoudeni Basin, West Africa, *in* Hambrey, M. J., and Harland, W. B., editors, Earth's Pre-Pleistocene Glacial Record: Cambridge, Cambridge University Press, p. 123–131.

Dorr, J. V. N., II, 1945, Manganese and iron deposits of Morro do Urucum, Mato Grosso, Brazil: U.S. Geological Survey Bulletin, v. 946-A, p. 1–47.

Foëlling, P. G., and Frimmel, H. E., 2002, Chemostratigraphic correlation of carbonate successions in the Gariep and Saldania Belts, Namibia and South Africa: Basin Research, v. 14, p. 69–88, doi: 10.1046/j.1365-2117.2002.00167.x.

Foëlling, P., Zartman, R. E., and Frimmel, H. E., 2000, A novel approach to double-spike Pb-Pb dating of carbonate rocks: examples from Neoproterozoic sequences in southern Africa: Chemical Geology, v. 171, p. 97–122, doi: 10.1016/S0009-2541(00)00204-7.

Font, E., Nedélec, A., Trindade, R. I. F., Macouin, M., and Charrière, A., 2006, Chemostratigraphy of the Neoproterozoic Mirassol d'Oeste cap dolostones (Mato Grosso, Brazil): An alternative model for Marinoan cap dolostone formation: Earth and Planetary Science Letters, v. 250, p. 89–103, doi: 10.1016/j.epsl.2006.06.047.

Frimmel, H. E., 2008, The Gariep Belt, *in* Miller, R. M., editor, The Geology of Namibia, Handbook of the Geological Survey of Namibia: Geological Survey of Namibia, p. 1–39.

——— 2010, On the reliability of stable carbon isotopes for Neoproterozoic chemostratigraphic correlation: Precambrian Research, "http://www.sciencedirect.com/scidirimg/clear.gif" doi: 10.1016/j.precamres.2010.01.003.

Frimmel, H. E., and Foëlling, P., 2004, Late Vendian closure of the Adamastor Ocean: Timing of tectonic inversion and syn-orogenic sedimentation in the Gariep Basin: Gondwana Research, v. 7, p. 685–699, doi: 10.1016/S1342-937X(05)71056-X.

Frimmel, H. E., Klötzli, U. S., and Siegfried, P. R., 1996, New Pb-Pb single zircon age constraints on the timing of Neoproterozoic glaciation and continental break-up in Namibia: Journal of Geology, v. 104, p. 459–469, doi: 10.1086/629839.

Frimmel, H. E., Zartman, R. E., and Spath, A., 2001, The Richtersveld Igneous Complex, South Africa, U-Pb Zircon and Geochemical Evidence for the Beginning of Neoproterozoic Continental Breakup: The Journal of Geology, v. 109, p. 493–508, doi: 10.1086/320795.

Frimmel, H. E., Foëlling, P. G., and Eriksson, P. G., 2002, Neoproterozoic tectonic and climatic evolution recorded in the Gariep Belt, Namibia and South Africa: Basin Research, v. 14, p. 55–67, doi: 10.1046/j.1365-2117.2002.00166.x.

Frimmel, H. E., and Von Veh, M. W., 2003, Numees Formation (Including the Jakkalsberg Member), *in* Johnson, M. R., editor, Catalogue of South African Lithostratigraphic Units: SA Committee for Stratigraphy, p. 25–27.

Gao, G., Dworkin, S. I., Land, L. S., and Elmore, R. D., 1996, Geochemistry of Late Ordovician Viola Limestone, Oklahoma: Implications for marine carbonate mineralogy and isotopic compositions: Journal of Geology, v. 104, p. 359–367, doi: 10.1086/629831.

Gaucher, C., Frimmel, H. E., and Germs, G. J. B., 2005, Organic-walled microfossils and biostratigraphy of the upper Port Nolloth Group (Namibia): implications for latest Neoproterozoic glaciations: Geological Magazine, v. 142, p. 539–559, doi: 10.1017/S0016756805001123.

Germs, G. J. B., and Gresse, P. G., 1991, The foreland basin of the Damara and Gariep Orogens in Namaqualand and southern Namibia: stratigraphic correlations and basin dynamics: South African Journal of Geology, v. 94, p. 159–169.

Grotzinger, J. P., Bowring, S. A., Saylor, B. Z., and Kaufman, A. J., 1995, Biostratigraphic and geochronologic constraints on early animal evolution: Science, v. 270, p. 598–604, doi: 10.1126/science.270.5236.598.

Halverson, G. P., 2006, A Neoproterozoic chronology, *in* Xiao, S., and Kaufman, A. J., editors, Neoproterozoic Geobiology and Paleobiology: New York, New York, Topics in Geology, v. 27, Springer, p. 231–271.

Halverson, G. P., Hoffman, P. F., Schrag, D. P., Maloof, A. C., and Rice, A. H. N., 2005, Toward a Neoproterozoic composite carbon-isotope record: Geological Society of America Bulletin, v. 117, p. 1181–1207, doi: 10.1130/B25630.1.

Halverson, G. P., Dudás, F. O., Maloof, A. C., and Bowring, S. A., 2007, Evolution of the $^{87}Sr/^{86}Sr$ composition of Neoproterozoic Seawater: Palaeogeography, Palaeoclimatology, Palaeoecology, v. 256, p. 103–129, doi: 10.1016/j.palaeo.2007.02.028.

Hoffman, P. F., and Li, Z.-X., 2009, A palaeogeographic context for Neoproterozoic glaciation: Palaeogeography, Palaeoclimatology, Palaeoecology, v. 277, p. 158–172, doi: 10.1016/j.palaeo.2009.03.013.

Hoffman, P. F., and Schrag, D. P., 2002, The snowball Earth hypothesis; testing the limits of global change: Terra Nova, v. 14, p. 129–155, doi: 10.1046/j.1365-3121.2002.00408.x.

Hoffmann, K.-H., Condon, D. J., Bowring, S. A., and Crowley, J. L., 2004, U-Pb zircon date from the Neoproterozoic Ghaub Formation, Namibia: constraints on Marinoan glaciation: Geology, v. 32, p. 817–820, doi: 10.1130/G20519.1.

Hoffman, P. F., Halverson, G. P., Domack, E. W., Husson, J. M., Higgins, J. A., and Schrag, D. P., 2007, Are basal Ediacaran (635 Ma) post-glacial "cap dolostones" diachronous?: Earth and Planetary Science Letters, v. 258, p. 114–131, doi: 10.1016/j.epsl.2007.03.032.

Ilyin, A. V., 2009, Neoproterozoic banded iron formations: Lithology and Mineral Resources, v. 44, p. 78–86, doi: 10.1134/S0024490209010064.

Jasper, M. J. U., Satanistreet, I. G., and Charlesworth, E. G., 2000, Neoproterozoic inversion tectonics, half-graben depositories and glacial controversies, Gariep fold-thrust belt, southern Namibia, *in* Miller, R. M., editor, Communications of the Geological Survey of Namibia, Henno Martin Commemorative Volume: Windhoek, Namibia, Geological Survey of Namibia, p. 1887–1896.

Jiafu, T., Fu, H., and Yu, Z., 1987, Stratigraphy, type and formation conditions of the Late Precambrian banded iron ores in South China: Chinese Journal of Geochemistry, v. 6, p. 332–351, doi: 10.1007/BF02872262.

Jiang, G., Kennedy, M. J., Christie-Blick, N., Wu, H., and Zhang, S., 2006, Stratigraphy, sedimentary structures, and textures of the late Neoproterozoic Doushantuo cap carbonate in South China: Journal of Sedimentary Research, v. 76, p. 978–995, doi: 10.2110/jsr.2006.086.

Kennedy, M. J., 1996, Stratigraphy, sedimentology, and isotope geochemistry of Australian Neoproterozoic postglacial cap dolostones: deglaciation, $\delta^{13}C$ excursions, and carbonate precipitation: Journal of Sedimentary Research, v. 66, p. 1050–1064.

Kianian, M., and Khakzad, A., 2008, Geochemistry of glacigenic Neoproterozoic banded iron formations from the Kerman District (Iran): Oslo, Norway, 33rd International Geological Congress, Abstracts, Session CGC-04.

Klein, C., and Beukes, N. J., 1993, Sedimentology and geochemistry of the glaciogenic late Proterozoic Rapitan iron-formation in Canada: Economic Geology, v. 88, p. 542–565, doi: 10.2113/gsecongeo.88.3.542.

Klein, C., and Ladeira, E. A., 2004, Geochemistry and mineralogy of Neoproterozoic banded iron-formations and selected, siliceous manganese formations from the Urucum District, Mato Grosso Do Sul, Brazil: Economic Geology, v. 99, p. 1233–1244, doi: 10.2113/99.6.1233.

Knoll, A. H., Javaux, E. J., Hewitt, D., and Cohen, P. A., 2006, Eukaryotic organisms in Proterozoic oceans: Philosophical Transactions of the Royal Society of London B: Biological Sciences, v. 361, p. 1023–1038, doi: 10.1098/rstb.2006.1843.

Kröner, A. W., 1974, The Gariep Group, Part I: Late Precambrian formations in the western Richtersveld, northern Cape Province: Cape Town, Precambrian Research Unit, University of Capetown, Bulletin, v. 13, p. 1–115.

Kump, L. R., and Seyfried, W. E., Jr., 2005, Hydrothermal Fe fluxes during the Precambrian: Effect of low oceanic sulfate concentrations and low hydrostatic pressure on the composition of black smokers: Earth and Planetary Science Letters, v. 235, p. 654–662, doi: 10.1016/j.epsl.2005.04.040.

Lottermoser, B. G., and Ashley, P. M., 2000, Geochemistry, petrology and origin of Neoproterozoic ironstones in the eastern part of the Adelaide Geosyncline, South Australia: Precambrian Research, v. 101, p. 49–67, doi: 10.1016/S0301-9268(99)00098-4.

Macdonald, F. A., Jones, D. S., and Schrag, D. P., 2009, Stratigraphic and tectonic implications of a newly discovered glacial diamictite-cap carbonate couplet in southwestern Mongolia: Geology, v. 37, p. 123–126, doi: 10.1130/G24797A.1.

Macdonald, F. A., Schmitz, M. D., Crowley, J. L., Roots, C. F., Jones, D. S., Maloof, A. C., Strauss, J. V., Cohen, P. A., Johnston, D. T., and Schrag, D. P., 2010, Calibrating the Cryogenian: Science, v. 327, p. 1241–1243, doi: 10.1126/science.1183325.

Martin, H., 1965a, Beobachtungen zum Problem der jung-Präkambrischen Glazialen Ablagerungen in Südwestafrika (Observations concerning the problem of the late Precambrian glacial deposits in South West Africa): Geologische Rundschau v. 54, p. 115–127, doi: 10.1007/BF01821173.

——— 1965b, The Precambrian geology of South West Africa and Namaqualand: Capetown, Precambrian Research Unit, University of Capetown, Bulletin, v. 4, p. 1–177.

McKirdy, D. M., Burgess, J. M., Lemon, N. M., Yu, X., Cooper, A. M., Gostin, V. A., Jenkins, R. J. F., and Both, R. A., 2001, A chemostratigraphic overview of the late Cryogenian interglacial sequence in the Adelaide fold-thrust belt, South Australia: Precambrian Research, v. 106, p. 149–186, doi: 10.1016/S0301-9268(00)00130-3.

McMillan, M. D., 1968, The geology of the Witputs-Sendelingsdrif area: Precambrian Research Unit, University of Capetown, Bulletin, v. 4, p. 1–177.

Mikucki, J. A., Pearson, A., Johnston, D. T., Turchyn, A. V., Farquhar, J., Schrag, D. P., Anbar, A. D., Priscu, J. C., and Lee, P. A., 2009, A contemporary microbially maintained subglacial ferrous "ocean": Science, v. 324, p. 397–400, doi: 10.1126/science.1167350.

Nogueira, A. C. R., Riccomini, C., Sial, A. N., Moura, C. A. V., and Fairchild, T. R., 2003, Soft-sediment deformaiton at the base of the Neoproterozoic Puga cap carbonate (southwestern Amazon craton, Brazil): Confirmation of rapid icehouse to greenhouse transition in snowball Earth: Geology, v. 31, p. 613–616, doi: 10.1130/0091-7613(2003)031<0613:SDATBO>2.0.CO;2.

Nogueira, A. C. R., Riccomini, C., Alcides, A. N., Moura, C. A. V., Trindade, R. I. F., and Fairchild, T. R., 2007, Carbon and strontium isotope fluctuations and paleoceanographic changes in the late Neoproterozoic Araras carbonate platform, southern Amazon craton, Brazil: Chemical Geology, v. 237, p. 168–190, doi: 10.1016/j.chemgeo.2006.06.016.

Prave, A. R., 1999, Two diamictites, two cap carbonates, two $\delta^{13}C$ excursions, two rifts; The Neoproterozoic Kingston Peak Formation, Death Valley, California: Geology, v. 27, p. 339–342, doi: 10.1130/0091-7613(1999)027<0339:TDTCCT>2.3.CO;2.

Prave, A. R., Fallick, A. E., Thomas, C. W., and Graham, C. M., 2009, A composite C-isotope profile for the Neoproterozoic Dalradian Supergroup of Scotland and Ireland: Journal of the Geological Society, London, v. 166, p. 845–857, doi: 10.1144/0016-76492008-131.

Preiss, W. V., 1987, The Adelaide Geosyncline: Late Proterozoic stratigraphy, sedimentation, paleontology and tectonics: Geological Survey of South Australia Bulletin, v. 53, 438 p.

Rogers, A. W., 1915, The geology of part of Namaqualand: Transactions of the Geological Society of South Africa, v. 18, p. 72–101.

Sawaki, Y., Ohno, T., Tahata, T., Komiya, T., Hirata, T., Maruyama, S., Windley, B. F., Han, J., Shu, D., and Li, Y., 2010, The Ediacaran radiogenic Sr isotope excursion in the Doushantuo Formation in the Three Gorges area, South China: Precambrian Research, v. 176, p. 46–64, doi: 10.1016/j.precamres.2009.10.006.

Shen, Y., Zhang, T., and Hoffman, P. F., 2008, On the co-evolution of Ediacaran oceans and animals: Proceedings of the National Academy of Sciences, v. 105, p. 7376–7381, doi: 10.1073/pnas.0802168105.

Shields, G. A., Deynoux, M., Strauss, H., Paquet, H., and Nahon, D., 2007, Barite-bearing cap dolostones of the Taoudéni Basin, northwest Africa: Sedimentary and isotopic evidence for methane seepage after a Neoproterozoic glaciation: Precambrian Research, v. 153, p. 209–235, doi: 10.1016/j.precamres.2006.11.011.

Stowe, C. W., Hartnady, C. J. H., and Joubert, P., 1984, Proterozoic tectonic provinces of Southern Africa: Precambrian Research, v. 25, p. 229–231, doi: 10.1016/0301-9268(84)90034-2.

Sumner, D. Y., and Bowring, S. A., 1996, U-Pb geochronologic constraints on deposition of the Campbellrand Subgroup, Transvaal Supergroup, South Africa: Precambrian Research, v. 79, p. 25–35, doi: 10.1016/0301-9268(95)00086-0.

Trompette, R., de Alvarenga, C. J. S., and Wade, D., 1998, Geological evolution of the Neoproterozoic Corumbá graben system (Brazil). Depositional context of the stratified Fe and Mn ores of the Jacadigo Group: Journal of South America Earth Sciences, v. 11, p. 587–597, doi: 10.1016/S0895-9811(98)00036-4.

Urban, H., Stribrny, B., and Lippolt, H. J., 1992, Iron and manganese deposits of the Urucum District, Mato Grosso do Sul, Brazil: Economic Geology, v. 87, p. 1375–1892, doi: 10.2113/gsecongeo.87.5.1375.

Von Veh, M. W., 1993, The stratigraphy and structural evolution of the Late Proterozoic Gariep Belt in the Sendelingsdrif-Annisfontein area, northwestern Cape Province: Capetown, Precambrian Research Unit, University of Capetown, Bulletin, v. 38, p. 1–174.

Wang, J., and Li, Z.-X., 2003, History of Neoproterozoic rift basins in South China: implications for Rodinia break-up: Precambrian Research, v. 122, p. 141–158, doi: 10.1016/S0301-9268(02)00209-7.

Xiao, S., Knoll, A. H., Yuan, X., and Pueschel, C. M., 2004, Phosphatized multicellular algae in the Neoproterozoic Doushantuo Formation, China, and the early evolution of florideophyte red algae: American Journal of Botany, v. 91, p. 214–227, doi: 10.3732/ajb.91.2.214.

Xu, B., Xiao, S., Zou, H.-B., Chen, Y., Li, Z.-X., Song, B., Liu, D.-Y., Zhou, C.-M., and Yuan, X.-L., 2009, SHRIMP zircon U-Pb age constraints on Neoproterozoic Quruqtah diamictites in NW China: Precambrian Research, v. 168, p. 247–258, doi: 10.1016/j.precamres.2008.10.008.

Yeo, G. M., 1981, The Late Proterozoic Rapitan glaciation in the northern Cordillera, *in* Campbell, F. H. A., editor, Proterozoic Basins of Canada: Geological Survey of Canada Paper 81–10, p. 25–46.

Yoshioka, H., Asahara, Y., Tojo, B., and Kawakami, S., 2003, Systematic variations in C, O, and Sr isotopes and elemental concentrations in Neoproterozoic carbonates in Namibia: implications for a glacial to interglacial transition: Precambrian Research, v. 124, p. 69–85, doi: 10.1016/S0301-9268(03)00079-2.

Young, G. M., 1976, Iron-formation and glaciogenic rocks of the Rapitan Group, Northwest Territories, Canada: Precambrian Research, v. 3, p. 137–158, doi: 10.1016/0301-9268(76)90030-9.